CHALMERS
UNIVERSITY OF TECHNOLOGY

Computation of Dark Matter Signals in Graphene Detectors

A numerical evaluation of the dark matter induced electron ejection rate under a constant, linear and quadratic relation between the scattering amplitude and the momentum transfer

Bachelor's thesis in the Engineering Physics Programme

Julia Andersson, Ebba Grönfors, Christoffer Hellekant, Ludvig Lindblad and Fabian Resare

Department of Physics
CHALMERS UNIVERSITY OF TECHNOLOGY
Gothenburg, Sweden 2020

Bachelor's thesis TIFX04-20-09

Computation of Dark Matter Signals in Graphene Detectors

A numerical evaluation of the dark matter induced electron ejection rate under a constant, linear and quadratic relation between the scattering amplitude and the momentum transfer

Julia Andersson, Ebba Grönfors, Christoffer Hellekant,
Ludvig Lindblad and Fabian Resare

CHALMERS
UNIVERSITY OF TECHNOLOGY

Department of Physics
Division of Subatomic, High Energy and Plasma Physics
Gothenburg, Sweden 2020

Computation of Dark Matter Signals in Graphene Detectors
A numerical evaluation of the dark matter induced electron ejection rate under a constant, linear and quadratic relation between the scattering amplitude and the momentum transfer

Authors: Julia Andersson[a], Ebba Grönfors[b], Christoffer Hellekant[c], Ludvig Lindblad[d] and Fabian Resare[e]

Contact:
[a]julande@student.chalmers.se
[b]gronfors@student.chalmers.se
[c]chrhelle@student.chalmers.se
[d]ludli@student.chalmers.se
[e]resaref@student.chalmers.se

Supervisors: Riccardo Catena, Department of Physics
Timon Emken, Department of Physics
Examiner: Jan Swensson, Department of Physics

Bachelor's Thesis 2020: TIFX04-20-09
Department of Physics
Division of Subatomic, High Energy and Plasma Physics
Chalmers University of Technology
SE-412 96 Gothenburg
Telephone +46 31 772 1000

Cover: Spiral galaxy (Andromeda Galaxy) providing some of the first strong indications of the existence of dark matter. Credit & Copyright: Robert Gendler [1]

Typeset in LaTeX
Printed by Chalmers Reproservice
Gothenburg, Sweden 2020

Abstract

Modern cosmology proposes the existence of some unknown substance constituting 85% of the mass of the universe. This substance has been named dark matter and has been hypothesised to be composed of an as of yet unknown weakly interacting particle. Recently, the use of graphene as target material for the direct detection of dark matter has been suggested. This entails the study of the dark matter induced ejection of graphene valence electrons. In this thesis, we calculate the rate of graphene valence electron ejection under the assumption of different dark matter models, specifically where the squared modulus of the scattering amplitude scales like $|\mathbf{q}|^2$ or $|\mathbf{q}|^4$, where $\mathbf{q}$ is the momentum transfer. These models have not previously been considered. We initially derive analytic expressions for the electron ejection rate of these models, which we then evaluate numerically through the use of *Python*. The ejection rate is then plotted as a function of the electron ejection energy. We find that the electron ejection rate declines less rapidly in the models studied here than in the case of a constant scattering amplitude, i.e. the only case previously studied. The main challenge in these calculations is the high complexity of multidimensional integrals, the evaluation of which necessitated approximately 15,000 core hours.

Keywords: Dark matter, WIMP, SHM, Graphene, Scattering amplitude, Electron ejection rate

Sammandrag

Modern kosmologi anför att det existerar någon okänd substans som utgör ungefär 85% av massan i universum. Denna substans kallas mörk materia och har hypotiserats bestå av hittills okända svagt interagerande partiklar. Nyligen har bruket av grafen som strålmål vid direkt detektion av mörk materia föreslagits. Denna metod innebär att valenselektronutstötning i grafen som inducerats av mörk materia studeras. I följande kandidatuppsats beräknar vi elektronutstötningshastigheten vid antagande av olika modeller för mörk materia, mer specifikt modeller där beloppet av spridningsamplituden i kvadrat är proportionell mot $|\mathbf{q}|^2$ eller $|\mathbf{q}|^4$, där $\mathbf{q}$ är överföringsrörelsemängden. Dessa modeller har aldrig tidigare studerats. Initialt härleder vi ett analytiskt uttryck för elektronutstötningshastigheten för dessa modeller, som vi därefter evaluerar numeriskt med hjälp av *Python*. Utstötningshastigheten plottas sedan som en funktion av elektronens utstötningsenergi. Vi erfar att utstötningshastigheten avtar långsammare för de studerade modellerna än då spridningsamplituden är konstant, d.v.s. det enda tidigare studerade fallet. Den främsta utmaningen i dessa beräkningar är den höga komplexiteten i de flerdimensionella integralerna, vars evaluering krävde ungefär 15 000 kärntimmar.

Nyckelord: Mörk materia, WIMP, SHM, Grafen, Spridningsamplitud, Elektronutstötningshastighet

Acknowledgements

We want to thank our supervisors Riccardo Catena and Timon Emken, without whom this thesis would never have been possible, for double checking our normalisation of wave functions, guiding us through the analytical derivation and aiding the very extensive troubleshooting of the code. We would also like to thank Andreas Ekström for helping with the Swedish translation of certain scientific terminology.

Julia Andersson, Ebba Grönfors, Christoffer Hellekant,
Ludvig Lindblad and Fabian Resare

Gothenburg, May 2020

Contents

Part I

A Swedish Summary of the Thesis

Bakgrund

Under 1900-talet observerades flera kosmologiska fenomen som trots introduktionen av den generella relativitetsteorin var oförklarliga. Allt fler tecken tydde på att universum innehåller en stor mängd odetekterad massa. Med bättre teknologi växte hypotesen om mörk materia (DM), och motsvarande DM-partiklar, fram [6].

Svagt växelverkande massiva partiklar (WIMP) är hypotetiska potentiella DM-partiklar. De antas vara icke-baryoniska och icke-relativistiska, samt enbart interagera med observerbar materia genom gravitation och svag växelverkan. WIMP-lika partiklar förutspås finnas i en förlängning av standardmodellen genom supersymmetri, där det för varje fermion finns en boson med samma kvanttal, och vice versa [14].

Standard Halo Model (SHM) är en hypotetisk modell som utgår från att DM följer samma gravitationella lagar som baryonisk materia och anför att DM samlas i hopar. Dessa hopar bildar gravitationella brunnar som baryonisk materia faller in i. Från SHM följer att DM-densiteten är högst i mitten av galaxer och att 85% av massan hos varje galax utgörs av DM [16].

För närvarande pågår, och planeras, experiment världen över i jakt på en DM-partikel. Nyligen har en ny realisation av direkt detektion, en av flera detektionsmetoder, som använder tvådimensionella strålmål föreslagits. Den främsta fördelen med denna metod är att den medför en direkt korrelation mellan DM-partikelns infallsriktning och elektronens utstötningsriktning, information som går förlorad i tredimensionella strålmål [20]. En detektorprototyp som kan realisera denna metod med grafen som strålmål, PTOLEMY, är för närvarande under utveckling [21].

Syfte och avgränsningar

Syftet med följande kandidatuppsats var att beräkna utstötningshastigheten för DM-inducerad elektronutstötning med grafen som strålmål. Utöver ett konstant samband mellan spridningsamplituden $\mathcal{M}$ och överföringsrörelsemängden $\mathbf{q}$ studerades även fallen $|\mathcal{M}|^2 \propto |\mathbf{q}|^2$ och $|\mathcal{M}|^2 \propto |\mathbf{q}|^4$. Enbart rent beroende av $\mathbf{q}$ undersöktes. Hela projektet har genomförts i enlighet med WIMP- och SHM-hypotesen.

Analytisk härledning av utstötningshastigheten

Ett explicit uttryck för utstötningshastigheten kan härledas analytiskt utifrån kvantmekanisk och matematisk teori. Vi börjar med att introducera en DM-partikel med rörelsemängd $\mathbf{p}$ och spinn s samt en elektron med rörelsemängd $\mathbf{k}$ och spinn r. Vi kan beteckna dessa partiklars initialtillstånd vid tidpunkten $t = -\infty$ med $|i\rangle$ samt sluttillstånd vid $t = +\infty$ med $|f\rangle$. Vi inför därefter tidsutvecklingsoperatorn S som avbildar $|i\rangle$ på $S\,|i\rangle$ vid tidpunkten $t = +\infty$. Matriselementet S_{fi} definieras enligt

$$S_{fi} = \frac{\langle f|\, S\,|i\rangle}{V^2}, \tag{0.1}$$

där $1/V^2$ är en normaliseringskonstant. Övergångsannolikheten från $|i\rangle$ till $|f\rangle$ ges enligt $P_{i\to f} = |S_{fi}|^2$. Vi kan nu definiera det differentiella tvärsnittet $d\sigma$ samt den differentiella utstötningshastigheten dR så att

$$dR = \frac{P}{T \cdot n} = \frac{PV}{T} = v_{rel} d\sigma, \tag{0.2}$$

där v_{rel} är DM-partikelns initialhastighet relativt jorden och n är DM-densiteten i fasrummet. Utstötningshastigheten kan alltså beräknas genom integration av ekvation (0.2). Vidare kan matriselementet S_{fi} uttryckas enligt

$$S_{fi} = (2\pi)^4 \delta^{(4)}(p' + k' - p - k) \frac{i\mathcal{M}}{\sqrt{2E_{\mathbf{p}} 2E_{\mathbf{k}} 2E_{\mathbf{p}'} 2E_{\mathbf{k}'}}}, \tag{0.3}$$

där $\mathcal{M} = \mathcal{M}(p', k', p, k)$ är elektronernas DM-inducerade spridningsamplitud [22]. Vi kan nu införa Hamiltonoperatorn i interaktionsbilden H_I och motsvarande Hamiltondensitet $\mathscr{H}$. Vidare kan initial- och sluttillståndet definieras enligt $|i\rangle = |\mathbf{p}, e_1\rangle$ och $|f\rangle = |\mathbf{p}', e_2\rangle$, vilket ger S_{fi} enligt

$$S_{fi} = \int d^3x \, \langle \mathbf{p}', e_2 | \, \mathscr{H}_S(x) \, | \mathbf{p}, e_1 \rangle \int_{-\infty}^{\infty} dt \, e^{i(E_f - E_i)t}. \tag{0.4}$$

Genom projektion på enhetsvektorerna kan vi nu införa tillståndsvektorerna $|\mathbf{k}\rangle$ och $|\mathbf{k}'\rangle$, som båda utgör kompletta baser för en fri elektron. Ekvation (0.3) ger då

$$S_{fi}^{free} = -i(2\pi)\delta(E_f - E_i) \, \langle \mathbf{p}', \mathbf{k}' | \int d^3x \mathscr{H}_S(x) \, | \mathbf{p}, \mathbf{k} \rangle \tag{0.5}$$

och jämförelse av dessa ekvationer kan användas för att förenkla det uttryck för S_{fi} som ges i ekvation (0.4). Vi inför dessutom rörelsemängdsöverföringen $\mathbf{q} = \mathbf{p} - \mathbf{p}' = \mathbf{k}' - \mathbf{k}$ samt ett ortogonalt komplement till denna, $\mathbf{v}_{\text{el}}^{\perp}$. Notera att eftersom $\mathbf{p}$ och $\mathbf{k}$ är linjärt oberoende kan vi definiera $\mathcal{M}(\mathbf{p} - \mathbf{q}, \mathbf{k} + \mathbf{q}, \mathbf{p}, \mathbf{k}) = \mathcal{M}(\mathbf{q}, \mathbf{v}_{\text{el}}^{\perp})$. Detta kan nu appliceras på ekvation (0.2) för att uttrycka den differentiella DM-inducerade elektronutstötningshastigheten. Om vi sedan integrerar detta uttryck över $\mathbf{q}$ och inför den reciproka gittervektorn $\boldsymbol{\ell}$ får vi ett uttryck för $v_{rel}\sigma(\boldsymbol{\ell}', \boldsymbol{\ell})$ enligt

$$v_{rel}\sigma(\boldsymbol{\ell}', \boldsymbol{\ell}) = \int_{\mathbf{q}} \frac{d^3q}{(2\pi)^3} (2\pi)\delta(E_f - E_i) \left| \int_{\mathbf{k}} \frac{d^3k}{(2\pi)^3} \psi_2^*(\boldsymbol{\ell}', \mathbf{k} + \mathbf{q}) \frac{\mathcal{M}(\mathbf{q}, \mathbf{v}_{\text{el}}^{\perp})}{4 m_\chi m_e} \psi_1(\boldsymbol{\ell}, \mathbf{k}) \right|^2 \tag{0.6}$$

där $\mathcal{M}(\mathbf{q}, \mathbf{v}_{\text{el}}^{\perp}) = (4\sqrt{\pi} m_\chi m_e / \mu_{e\chi}) \sqrt{\bar{\sigma}_e} F_{DM}(\mathbf{q}, \mathbf{v}_{\text{el}}^{\perp})$ [20]. Här betecknar m_χ och m_e massan för en DM-partikel respektive elektron, $\mu_{e\chi}$ den reducerade massan, och $\bar{\sigma}_e$ ett referenstvärsnitt. Detta sätts in i ekvation (0.6), vilket ger ett uttryck för utstötningshastigheten som sedan kan specificeras för utstötning av valenselektroner i grafen genom interaktioner med DM-partiklar. Tillståndet för en utstött elektron kan beskrivas som en plan våg i positionsrummet. Detta kan implementeras i uttrycket för $v_{rel}\sigma(\boldsymbol{\ell}', \boldsymbol{\ell})$, som därefter kan Fouriertransformeras från en integral över rörelsemängden $\mathbf{k}$ till en integral över rumskoordinaten $\mathbf{x}$. Resultatet av detta är detsamma som Fouriertransformen $\psi(\boldsymbol{\ell}, \mathbf{q} - \mathbf{k}_f)$. Vi kan använda detta uttryck för

att omformulera ekvation (0.6). Vi multiplicerar även med $\frac{d^3k_\mathrm{f}}{(2\pi)^3}V$ för att senare kunna summera över alla slutgiltiga elektronrörelsemängder $\mathbf{k}_\mathrm{f}$. Detta ger att

$$v_{rel}\sigma(\boldsymbol{\ell},\boldsymbol{\ell}') = \frac{\bar{\sigma}_e}{\mu_{e\chi}^2}\int_{\mathbf{q}}\frac{d^3q}{4\pi}\int_{\mathbf{k}_\mathrm{f}}\frac{d^3k_\mathrm{f}}{(2\pi)^3}\left|F_{DM}(\mathbf{q},\mathbf{v}_\mathrm{el}^\perp)\right|^2\left|\tilde{\psi}_1(\boldsymbol{\ell},\mathbf{q}-\mathbf{k}_\mathrm{f})\right|^2\times\delta(E_f-E_i). \quad (0.7)$$

Vi noterar att detta uttryck är ekvivalent med ekvation (5) i [20]. Slutligen summerar vi över de fyra valenselektronerna hos grafen med hänsyn till spindegenerationen hos varje band, vilket ger

$$R = 2\sum_{i=\pi,\sigma_1,\sigma_2,\sigma_3}\frac{\rho_\chi}{m_\chi}N_C A_{uc}\int_{1\mathrm{BZ}}\frac{d^2\ell}{(2\pi)^2}d^3v g(\mathbf{v})v_\mathrm{rel}\sigma_i(\boldsymbol{\ell}). \quad (0.8)$$

Värden för samtliga kända storheter anges i enligthet med [20] och [23].

Hittills har vi antagit att $\mathcal{M}$ är oberoende av rörelsemängdsöverföringen $\mathbf{q}$, i enlighet med [20], och definierat formfaktorn därefter. Detta behöver dock inte vara fallet. $\mathcal{M}$ måste uppfylla invarians vid translation i rummet, vid tredimensionella rotationer och vid Galileitransformationer. Under dessa villkor kan $\mathcal{M}$ skrivas som en linjärkombination av 14 olika termer beroende av $\mathbf{q}$, $\mathbf{v}_\mathrm{el}^\perp$, $\mathbf{S}_e$ och $\mathbf{S}_\chi$, vilka finns givna i [24]. Från detta följer att fallen $|\mathcal{M}|^2\propto|\mathbf{q}|^2$ och $|\mathcal{M}|^2\propto|\mathbf{q}|^4$, bland andra, även kan beräknas.

Beräkning av utstötningshastigheten

I syfte att effektivisera den numeriska utvärderingen av utstötningshastigheten i ekvation (0.8) kan ett antal omskrivningar genomföras. Notera först att eftersom enbart kontaktinteraktioner betraktas låter vi $F_{DM}=1$. Därefter kan volymintegralen över v skrivas om i sfäriska koordinater projicerade på överföringsrörelsemängdens riktning. Utstötningshastigheten kan då skrivas enligt

$$\frac{dR}{d\ln(E_{er})} = 2\sum_\mathrm{band}\frac{\rho_\chi N_c A_{uc}\bar{\sigma_e}}{m_\chi\mu_{e\chi}^2}\int_{1\mathrm{BZ}}\frac{d^2\ell}{(2\pi)^2}\int_{\Omega_{k_\mathrm{f}}}\frac{d\Omega_{k_\mathrm{f}}}{(2\pi)^3}\frac{k_\mathrm{f}^3}{(2\pi)^2}\int_{q_\mathrm{min}}^{q_\mathrm{max}}\frac{d^3q}{4\pi}\frac{\pi}{q}\eta(v_\mathrm{min})\left|\tilde{\psi}_i(\boldsymbol{\ell},\mathbf{q}-\mathbf{k}_\mathrm{f})\right|^2 \quad (0.9)$$

där $\eta(v_\mathrm{min})$ definieras enligt

$$\eta(v_\mathrm{min}) = \int_{\Omega_{qv}}d\Omega_{qv}\int_{v>v_\mathrm{min}}dvvg(v). \quad (0.10)$$

Summan löper över elektronbanden i grafen $\pi,\sigma_1,\sigma_2,\sigma_3$. Notera att $\eta(v_\mathrm{min})$ kan utvärderas analytiskt. När dessa omskrivningar genomförts kvarstår vågfunktionerna för valenselektronerna i grafen. Den stationära Schrödingerekvationen för vågfunktionerna kan formuleras enligt

$$\mathcal{H}\mathbf{C} = E_i(\boldsymbol{\ell})\mathcal{S}\mathbf{C}, \quad (0.11)$$

där $\mathcal{H}$ är en överföringsmatris och $\mathcal{S}$ är en överlappsmatris, för varje energiband i. Bandenergin för respektive band kan beräknas genom att lösa ekvation (0.11). Därefter kan motsvarande egenvektor $\mathbf{C}$ beräknas. Både bandenergierna och egenvektorerna tabellerades över ett rutnät i det reciproka rummet. Blochvågfunktionerna normaliserades därefter analytiskt med hjälp av de tabellerade värdena.

Efter de förberedande stegen implementerades uttrycket för ekvation (0.9), och samtliga tabellerade värden, i *Python* för numerisk beräkning av utstötningshastigheten. Mer specifikt genomfördes detta genom att betrakta $\mathbf{k}_\mathrm{f}$ i en loop. För varje $\mathbf{k}_\mathrm{f}$ evaluerades en lambda-funktion för gittervektorn $\boldsymbol{\ell}$. Denna integrerades sedan över rörelsemängdsrummet $\mathbf{q}$ och differentialvinkeln Ω_{k_f}, vilket skapade en matris i reciproka rummet över första Brillouinzonen. Påföljande integration över första Brillouinzonen evaluerades som en summa multiplicerat med differentiella areaelementet $d^2\ell$. Detta gav den slutgiltiga numeriska evalueringen av ekvation (0.9) för ett givet $\mathbf{k}_\mathrm{f}$. Utstötningshastigheten kunde till sist plottas som en funktion av kinetiska energin $E_{er} = k_\mathrm{f}^2/2m_e$. Modifikationen av spridningsamplituden genomfördes genom att omdefiniera formfaktorn enligt $F_{DM} = A_1|\mathbf{q}|$ respektive $F_{DM} = A_2|\mathbf{q}|^2$, där A_1 och A_2 är okända modellparametrar. I dessa fall ansattes parametrarna så att utstötningsfaktorn fick samma startvärde för samtliga fall.

Resultat

I Figur 0.1 ses den totala utstötningshastigheten för samtliga atomband som en funktion av E_{er} för varje undersökt fall, dvs $|M|^2 \propto 1$, $|M|^2 \propto |\mathbf{q}|^2$ och $|M|^2 \propto |\mathbf{q}|^4$.

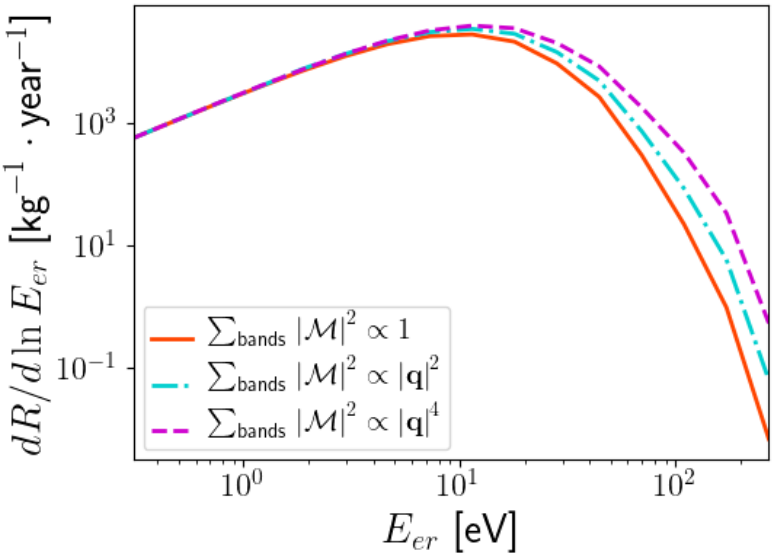

Figur 0.1: Den totala differentiella utstötningshastigheten för en inkommande DM-partikel med m_χ=100 MeV och $\bar{\sigma}_e = 10^{-37}\mathrm{cm}^2$, för varje spridningsamplitud. Utstötningshastigheten plottas som en funktion av den kinetiska energin hos de utstötta elektronerna, E_er. Det kan ses att utstötningshastigheten avtar långsammare för högre potenser av $|\mathbf{q}|$.

Här framgår att den primära skillnaden mellan de olika fallen är att för $|\mathbf{q}|$ av högre grad följer det att utstötningshastigheten avtar långsammare då E_{er} ökar. Vidare finns en oanselig skillnad i energin för vilken utstötningshastigheten maximeras mellan de olika fallen.

Diskussion

Det är väsentligt att notera att storleken av utstötningshastigheten är godtycklig för samtliga studerade fall, eftersom $\bar{\sigma}_e$, A_1 och A_2 är okända modellparametrar. Detta innebär att komparativa slutsatser nödvändigtvis måste dras från kurvornas kvalitativa egenskaper. Även analys av eventuell experimentell mätdata bör utgå från kurvornas beteende snarare än storlek. Som tidigare nämnts är den huvudsakliga skillnaden mellan de olika fallen att utstötningshastigheten avtar långsammare då $|\mathbf{q}|$ har högre potens. Dessutom förskjuts kurvans maxvärde något åt höger. Dessa skillnader är väntade eftersom $|\mathbf{q}|$ ökar med ökande elektronenergi, vilket utstötningshastigheten nu är mer dominant beroende av. Dessa typer av beroende har aldrig tidigare undersökts, och implementationen av dem bidrar därför direkt till forskning inom detektion av DM-partiklar.

En genomgående problematik för detta projekt var beräkningsrestriktioner. Ett flertal metoder undersöktes och applicerades i syfte att motverka dem. Dock kvarstod problemet i viss mån även i den slutgiltiga metoden. Initialt jämfördes olika bibliotek för integration i *Python*, i syfte att finna den mest effektiva. I slutändan identifierades *mpmath* som det med bäst prestanda, vilket sedan användes genom arbetet. Vidare genomfördes ett försök att med hjälp av biblioteket *Cython* kompilera koden som *C*-kod och därigenom förkorta exekveringstiden. Eftersom *mpmath* är skrivet i *Python* gav detta ingen betydelsefull förbättring. Ett ytterligare tillvägagångssätt var parallellisering av koden, där beräkningen fördelades över olika k_{f}. Ytterligare samtidig parallellisering av $\boldsymbol{\ell}$ hade krävt fördelning av matriser mellan kärnor, något som hade komplicerat programmet avsevärt.

Som tidigare nämnts har endast fall då $\mathcal{M}$ enbart beror av $\mathbf{q}$ undersökts. Mer explicit har beroende av $\mathbf{v}_{\mathrm{el}}^{\perp}$ utelämnats. Skulle detta utelämnande hävas hade antalet beräkningsbara interaktionstyper ökat. Konkret hade detta inneburit att interaktioner mellan DM-partiklar och valenselektroner i grafen i fall då DM-partiklarna modelleras som toroida (*eng. anapole*), elektriska och magnetiska dipoler kan undersökas. Notera att detta skulle kräva en markant ökning av beräkningskapaciteten. Vidare skulle integralen över hastighet $\mathbf{v}$ inte längre vara analytiskt evaluerbar.

Part II

Thesis

1
Introduction

As cosmological theory and technology have progressed the existence of undetected matter in the universe has become increasingly apparent and ultimately irrefutable. This unidentified substance is now known as dark matter and the exact nature of this substance is yet to be determined. Several detection experiments are currently being developed and performed worldwide. In order to enable accurate data analysis from these experiments, computational simulations of interactions between dark matter and target materials are being performed as well. In the following chapter the history of dark matter is presented, as well as a summary of the contemporary state of dark matter detection techniques and research. Finally, a specific detection method using graphene as target material is explained, especially in regard to the purpose of the following thesis.

1.1 A Brief History of Dark Matter

In 1687 Isaac Newton forever changed our understanding of the cosmos when he published his law of gravity [2]. This theory can, in great detail, describe the planetary orbits. It does, however, fail to explain the small variations observed in for example the orbit of Mercury. This was later resolved by general relativity, published by Albert Einstein in 1915 [3]. As astronomic knowledge progressed, astronomers gradually developed a cosmological model of the universe. However, throughout the 19th and 20th century, astronomers continually made as of yet inexplicable observations. Slowly, a hypothesis of some unknown, invisible cosmological substance began to form.

More and more signs of this unknown substance emerged. Astronomers studied the uneven distribution of stars and pondered the space between them. Did the dark regions arise due to the scarcity of stars, or some absorbing matter? While still speculative at best, the idea of dark matter began to gain traction. The first to attempt an estimation of the amount of dark matter was Lord Kelvin. He regarded stellar systems in the galaxy as particles in a gas and applied the thermodynamic models this assumption entailed. In doing this he was able to establish a relation between the size of a galaxy and the velocity dispersion of the stars, as well as an upper limit of the mass density. This work inspired the French astronomer Henri Poincaré, who based on this result argued that the amount of dark matter should be less than or equal to that of visible matter [4]. This result was later countered by another astronomer, Fritz Zwicky, who during the 1930s studied the redshift of

galaxy clusters. As a result of these studies, Zwicky estimated the total mass, as well as the observable luminous mass, of the clusters. He subsequently calculated the mass-to-light ratio to be approximately 500 [5]. Further estimations would later be added to the list and little agreement could be found within the astronomical community. Despite this, one thing was becoming increasingly clear: dark matter exists [6].

As cosmological studies advanced, the evidence for the existence of invisible, undetected matter accumulated. In the late 1930s, astronomer Horace Babcock studied the rotation curve of the Andromeda Galaxy. He reported an estimated mass-to-light ratio of 50. However, his report suggested something much more consequential. He seemed to have discovered that the mass-to-light ratio increased radially. Moreover, Babcock measured an inexplicably high circular velocity at large radii. This all seemed to suggest a large amount of mass in the outer parts of galaxies. A model lacking dark matter is unable to account for these results [7]. As more powerful technologies developed, the 1970s proved to be a revolutionary time in the field of dark matter. Among others, astronomers Vera Rubin and Kent Ford used a new optical spectrometer. Their results, which were later confirmed in 1978, showed that most galaxies must contain about 6 times more mass than has been detected [8]. Concurrently, astrophysicist Ken Freeman compared the radii at which galactic rotation curves were theoretically predicted to peak with photometric observations. His remarkable findings were that the rotation curves peaked at a larger radii than predicted, and thus concluded that galaxies must contain more mass than what was detectable [9]. The evidence for dark matter was becoming progressively indisputable. As cosmology advanced, further evidence emerged in other phenomena, such as the cosmic microwave background [10] and gravitational lensing [11].

The overwhelming evidence of the existence of undetected mass eventually prompted a well-established use of the term dark matter (DM) as a hypothesis to explain the discrepancy between the observable luminous matter and the matter needed to sustain the gravitational attraction necessary in the outermost region of spiral galaxies. A term that had previously been used as a vague description of some ambiguous physical phenomenon transformed into a specific substance, with at least some well-known properties. It was evident that DM interacts with regular matter through gravity, but not through the electromagnetic force. Speculation regarding the exact nature of the elusive substance quickly arose. The hypothesis of a DM particle emerged. Suddenly, the DM problem was no longer strictly in the hands of astronomy, but particle physics as well. The Standard Model of particle physics was closely examined in search of a potential DM particle. Unlike other particles, neutrinos are long lived and do not interact with other matter through electromagnetic or strong force. Based on this, neutrinos quickly became the primary DM candidate [12]. However, by the middle of the 1980s numerical calculations could be used to simulate how a large number of DM particles behave in an expanding universe. The role of DM in the formation of large cosmological structures could be evaluated and the results showed that neutrinos were no longer realistic as DM particles, as DM is known to be cold and due to the extremely small rest mass of neutrinos, they are

necessarily hot [13]. As neutrinos had been the only known feasible DM candidate, particle physicists started to entertain the thought of extending the Standard Model. The idea of weakly interacting massive particles emerged and quickly became the leading hypothesis.

The history of dark matter has reflected the history of cosmological and technological progress. As the knowledge and tools of astronomy progressed, the idea of dark matter transformed from a vague speculation of something unknown into a well defined hypothesis, and acceptance of the DM hypothesis grew rapidly. What remains is definite proof, i.e. detection. As of today, any still viable DM candidate has yet to be detected. The future of particle physics will thus be determined by the results of the countless detection experiments being performed and developed worldwide.

1.2 Contemporary State of Dark Matter Research

In the following sections two hypotheses of the composition and distribution of DM, as well as the current state of DM detection, is presented. Both of the described hypotheses are assumed throughout the remainder of this thesis.

1.2.1 Weakly Interacting Massive Particles

Weakly interacting massive particles (WIMPs) are hypothetical particles. They are assumed to interact with observable luminous matter through gravity and weak nuclear force only, and to be non-baryonic and cold. Non-baryonic matter is matter that is not made up of baryons, i.e. particles composed of an odd number of quarks, and a cold particle species is non-relativistic. WIMP-like particles are predicted to exist through a so called supersymmetric extension of the Standard Model. Supersymmetry is a spacetime symmetry stating that for every fermion there exists a boson with the same quantum numbers, and vice versa. This would entail a number of electrically neutral, weakly interacting particles. Any such particle that is stable could be cosmologically abundant and thus a likely DM candidate. No such particle has as of yet been detected [14]. DM detection will be discussed in greater detail in Section 1.2.3.

1.2.2 Standard Halo Model

As has been discussed, galaxies and galaxy clusters have been a great source for evidence of the existence of DM. As cosmological studies advanced it became clear that DM played an important role in the formation and structure of galaxies. In regard to this, the so called Standard Halo Model of DM (SHM), modelling the velocity distribution of DM particles, has been gaining wider acceptance. Working from the widely held belief that DM obeys gravitational laws the same way as baryonic matter, this hypothesis states that DM clumps and clusters around galaxies, forming gravitational wells which baryonic matter falls into. These overdensities then contain the galaxy. Under the simplifying assumptions that the halo density

is spherical, the DM distribution is smooth and the halo is isothermal, it can be shown that $M(r) \propto r$ and $\rho(r) \propto r^{-2}$, where $M(r)$ is the total DM mass within the radius r and $\rho(r)$ is the radial DM distribution. This entails that the density of DM is largest in the center of galaxies. As it turns out, the distribution $\rho(r)$ approximately fits and explains the studied behaviour of the rotational curve [15]. Consequently, this implies that galaxies must consist of about 85% DM for the halo model to conform [16].

1.2.3 Dark Matter Detection

The experimental detection of DM particles is necessary in order to confirm the WIMP hypothesis. Since there is no electromagnetic interaction between DM and baryonic matter, physicists are unable to observe DM by conventional means. This does not mean DM is undetectable, even though it has yet to be detected directly. Presently, the primary methods of DM detection are direct detection, in-direct detection and collider searches [6]. Direct detection experiments search for signals of DM–nucleus or DM–electron interactions in underground detectors. This is, for instance, attempted in the XENON research project at the Gran Sasso National Laboratory in Italy [17]. Indirect detection experiments search for particles, such as photons or positrons, produced by DM annihilations in our galaxy, or in nearby satellite galaxies. This is, for example, attempted using pair-conversion telescopes with the Fermi Large Area Telescope [18]. Collider searches are performed in particle accelerators by searching for DM production signals in the final state of proton–proton collisions. The ATLAS detector at CERN uses the Large Hadron Collider to attempt this method of detection [19]. None of these methods have thus far reported any unambiguous detection of DM particles.

Very recently a new realisation of the direct detection method has been suggested. It relies on the use of two-dimensional materials, such as graphene, as detector targets. In an experiment based on this method, the energy deposited in the detector by DM-electron scattering can cause the ejection of valence-band electrons from the graphene target. The energy and direction of the ejected electron can be measured with a combination of position, time-of-flight, and energy deposition measurements. The main advantage of using graphene is that it is two-dimensional. This entails a direct correlation between the direction of the incoming DM particle and the direction of the ejected electron, which would be lost via secondary electron scatterings in 3D target materials [20]. Furthermore, since this method utilises ejection of electrons, rather than nuclear recoils, it enables the detection of lower energy depositions than previous experimental setups. A prototype of an experiment that can realise this suggested method, PTOLEMY, is currently in a research and developmental stage. The PTOLEMY detector, like the XENON research project, is located in the Gran Sasso National Laboratory [21].

In a 2017 publication of a proposed experimental method, implementable in the PTOLEMY detector, Yonit Hochberg et al. [20] derived a numerical approximation for the DM induced ejection rate of graphene valence electrons, based on a number

of assumptions. Most notable is the assumption that the scattering amplitude $\mathcal{M}$ is independent of the momentum transfer $\mathbf{q} = \mathbf{p} - \mathbf{p}'$, where $\mathbf{p}$ and $\mathbf{p}'$ are the initial and final DM momenta.

1.3 Purpose Statement and Limitations

The purpose of this thesis was to compute the DM induced electron ejection rate in direct detection experiments using graphene as a target material, as in the case of the proposed PTOLEMY detector. Previous studies on the same topic have worked under the assumption of a constant dependence of the scattering amplitude on the momentum transfer. In this thesis this assumption has been lifted and the cases of $|\mathcal{M}(\mathbf{q})|^2 \propto |\mathbf{q}|^2$ and $|\mathcal{M}(\mathbf{q})|^2 \propto |\mathbf{q}|^4$ have been studied as well. These scattering amplitudes are expected in models where DM particles are regarded as fermions and interact with electrons via the exchange of pseudo-scalar particles, or in models where DM has spin 0 and interactions violate parity and charge conjugation parity. The point of studying these models is to produce theoretical results with which to compare future experimental data. From these comparisons conclusions can be drawn regarding the properties of DM particles. Due to the numerical unfeasibility within the scope of this thesis as well as time limitation, the dependence on any other contribution of DM particle momenta has not been regarded. All assumptions have been made in accordance with the WIMP and SHM hypotheses, see sections 1.2.1 and 1.2.2 respectively.

2
Analytical Derivations

The intention of the following chapter is to present a theoretical background and an analytical derivation of the rate of DM particle induced electron ejection. This rate will be evaluated numerically in the forthcoming chapters. To achieve the analytical expression for the rate we start by introducing a time evolution operator to our initial and final states and thereupon apply a Hamiltonian density in the interaction picture as well as a scattering amplitude. This will eventually generate the ejection rate through some analytical manipulation. By convention, everything is expressed in terms of natural units.

2.1 Rate of Electronic Ejection

The behaviour of the DM–electron interactions are highly dependent on whether the electrons are bound or not. In this case, we are mainly interested in bound electrons. However, as we will see, the forthcoming analytical derivation is somewhat simplified by studying DM interactions with free electrons first. For this reason, both cases are considered in succession in the following sections.

2.1.1 Dark Matter Particle Interactions with Free Electrons

We will start by introducing a notation for the linearly independent states of free particles, where $|\mathbf{p}, s\rangle$ describes a DM particle with momentum $\mathbf{p}$ and spin s while $|\mathbf{k}, r\rangle$ describes an electron with momentum $\mathbf{k}$ and spin r. From the definition of scalar products it follows that

$$\begin{aligned} \langle \mathbf{p}', s' | \mathbf{p}, s \rangle &= (2\pi)^3 \delta^{(3)}(\mathbf{p}' - \mathbf{p}) \delta_{ss'} \\ \langle \mathbf{p}, s | \mathbf{p}, s \rangle &= (2\pi)^3 \delta^{(3)}(0) = \int d^3x = V, \end{aligned} \tag{2.1}$$

where V is the volume of three-dimensional space. While formally divergent, it will disappear in our final results. The combined DM–electron states at times $t = +\infty$ and $t = -\infty$ can be expressed by the tensor product between the state vector of the DM particle and the state vector of the electron at $t = +\infty$ and $t = -\infty$, i.e.

$$\begin{aligned} |i\rangle &= |\mathbf{p}, s\rangle \otimes |\mathbf{k}, r\rangle = |\mathbf{p}, s, \mathbf{k}, r\rangle \\ |f\rangle &= |\mathbf{p}', s'\rangle \otimes |\mathbf{k}', r'\rangle = |\mathbf{p}', s', \mathbf{k}', r'\rangle \,. \end{aligned} \tag{2.2}$$

We let $|i\rangle$ and $|f\rangle$ denote the initial and final state, respectively. We now introduce the S matrix, which is the time evolution operator that maps $|i\rangle$ onto $S\,|i\rangle$ at

$t = +\infty$. We define the matrix element S_{fi} as

$$S_{fi} = \frac{\langle f| S |i\rangle}{V^2}, \tag{2.3}$$

where $1/V^2$ acts as normalisation. The probability of a transition from the initial state $|i\rangle$ to the final state $|f\rangle$ is then

$$P_{i\to f} = |S_{fi}|^2 = \frac{|\langle f| S |i\rangle|^2}{V^4}. \tag{2.4}$$

After introducing the momentum transfer $\mathbf{q} = \mathbf{p} - \mathbf{p}' = \mathbf{k}' - \mathbf{k}$, the total probability is thus given as

$$P(\mathbf{p}) = \frac{|S_{fi}|^2}{V^4} \cdot V \frac{d^3p'}{(2\pi)^3} = \frac{|S_{fi}|^2}{V^4} \cdot V \frac{d^3q}{(2\pi)^3}, \tag{2.5}$$

where the differential terms are the number of particles around the respective momentum. A differential cross section can be defined as

$$d\sigma = \frac{P}{T \cdot Flux}, \tag{2.6}$$

where T is the formally divergent factor, $T = \int dt$. Analogously to V, it will not appear in our final results. A cross section is a measure of the probability that certain particles, in this case DM particles and electrons, interact. We can now define the differential ejection rate as

$$dR = \frac{P}{T \cdot n} = \frac{PV}{T} = v_{rel} d\sigma, \tag{2.7}$$

where v_{rel} is the initial velocity of a DM particle, relative to the observer on earth, and n is the number density of the DM particles. By applying equation (2.5) onto (2.7), and subsequently integrating that expression, we get the ejection rate as

$$R = v_{\text{rel}}\sigma = \int_{\mathbf{q}} \frac{|S_{fi}|^2}{V^2 T} \frac{d^3q}{(2\pi)^3}. \tag{2.8}$$

We will remember this result for later and momentarily focus on the transition from $|i\rangle$ to $|f\rangle$ through S_{fi}. In accordance with [22], S_{fi} can be expressed as

$$S_{fi} = (2\pi)^4 \delta^{(4)}(p' + k' - p - k) \frac{i\mathcal{M}}{\sqrt{2E_{\mathbf{p}} 2E_{\mathbf{k}} 2E_{\mathbf{p}'} 2E_{\mathbf{k}'}}} \tag{2.9}$$

where $\mathcal{M} = \mathcal{M}(p', k', p, k)$ is the DM induced electron scattering amplitude and E_j, $j = p', k', p, k$, are energies. Here, $\mathcal{M}$ is a complex value such that the absolute square of the amplitude gives the probability of an electron transitioning from $|i\rangle$ to $|f\rangle$. The absolute square of S_{fi} can now be calculated, resulting in

$$|S_{fi}|^2 = \frac{|\mathcal{M}|^2}{16 E_{\mathbf{p}} E_{\mathbf{k}} E_{\mathbf{p}'} E_{\mathbf{k}'}} \left|(2\pi)^4 \delta^{(4)}(p' + k' - p - k)\right|^2. \tag{2.10}$$

By definition

$$\delta^{(4)}(p' + k' - p - k) = \int \frac{d^4x}{(2\pi)^4} e^{i(p'+k'-p-k)\cdot x}. \tag{2.11}$$

Note that the delta function in equation (2.11) is four dimensional. We now have,

$$\begin{aligned}
&\left|(2\pi)^4\delta^{(4)}(p' + k' - p - k)\right|^2 = \\
&= \left[(2\pi)^4 \left(\int \frac{d^4x}{(2\pi)^4} e^{i(p'+k'-p-k)\cdot x}\right)\right] (2\pi)^4\delta^{(4)}(p' + k' - p - k) = \\
&= \int d^4x (2\pi)^4\delta^{(4)}(p' + k' - p - k) = \\
&= TV(2\pi)^4\delta^{(4)}(p' + k' - p - k),
\end{aligned} \tag{2.12}$$

By combining equations (2.4), (2.10) and (2.12), the transition probability from $|i\rangle$ to $|f\rangle$ for one DM particle and one electron is given as

$$P_{i\to f} = \frac{T}{V^3}(2\pi)^4\delta^{(4)}(p' + k' - p - k)\frac{|\mathcal{M}|^2}{16E_{\mathbf{p}}E_{\mathbf{k}}E_{\mathbf{p}'}E_{\mathbf{k}'}}. \tag{2.13}$$

This expression can now be used to calculate the ejection rate in the case of DM particle interaction with free electrons, in accordance with equations (2.6) and (2.8). This will, however, not be necessary for the purpose of this thesis.

2.1.2 Bound Graphene Valence Electrons

The interactions studied thus far have been between a DM particle and a free electron. Let us now consider the case of an electron bound in graphene. We can once again apply a time evolution operator to an initial and final state, now according to

$$S_{fi} = -i \langle f| H_I |i\rangle . \tag{2.14}$$

Here, H_I is the Hamiltonian given in the Interaction picture, which is a formulation of quantum mechanics where both states and operators are dependent on time. By definition, a state vector in the Interaction picture is given by

$$|\psi_I\rangle = e^{H_{0,S}t} |\psi_S(t)\rangle , \tag{2.15}$$

where $|\psi_S(t)\rangle$ is a state vector and $H_{0,S}$ is an interaction free Hamiltonian. The subindex S signifies that these are given in the Schrödinger picture, i.e. the quantum mechanical formulation where states are dependent on time, but operators are not. Furthermore, the Hamiltonian in the Interaction picture is given by

$$H_I = e^{iH_{0,S}t} H_S(x) e^{-iH_{0,S}t}, \tag{2.16}$$

where $H_S(x)$ is the Hamiltonian in the Schrödinger picture. The Hamiltonian can also be described as a function of the Hamiltonian density $\mathscr{H}_I$ as

$$H_I = \int d^4x \mathscr{H}_I(x). \tag{2.17}$$

By applying equations (2.16) and (2.17) on equation (2.14), S_{fi} can now be expressed as

$$S_{fi} = -i \langle f | e^{iH_0 t} \int d^4x \mathscr{H}_I(x) e^{-iH_0 t} | i \rangle . \tag{2.18}$$

We define H_0 as the Hamiltonian for the system with no interaction, i.e. $H_I = 0$, and thus the total Hamiltonian for the system is given as

$$H_{tot} = H_0 + H_I. \tag{2.19}$$

When $t \to \pm\infty$, the interaction Hamiltonian will approach 0. Since energy is the eigenvalue of the Hamiltonian, it follows that

$$\begin{aligned} H_{tot} | i \rangle &= H_0 | i \rangle = E_i | i \rangle \\ H_{tot} | f \rangle &= H_0 | f \rangle = E_f | f \rangle . \end{aligned} \tag{2.20}$$

We now introduce a new notation for our initial and final states as

$$\begin{aligned} | i \rangle &= | \mathbf{p}, e_1 \rangle \\ | f \rangle &= | \mathbf{p}', e_2 \rangle , \end{aligned} \tag{2.21}$$

where e_1 and e_2 are the initial and final states of the electron, respectively. If we use this new notation, and split up the four dimensional integral in equation (2.18) into three dimensions of space and one dimension of time, S_{fi} can be written as

$$S_{fi} = \int d^3x \langle \mathbf{p}', e_2 | \mathscr{H}_S(x) | \mathbf{p}, e_1 \rangle \int_{-\infty}^{\infty} dt \, e^{i(E_f - E_i)t}. \tag{2.22}$$

S_{fi} can be manipulated further by inserting the so called resolution of the identity, given by

$$\mathbb{1} = \int \frac{d^3k}{(2\pi)^3} | \mathbf{k} \rangle \langle \mathbf{k} | = \int \frac{d^3k'}{(2\pi)^3} | \mathbf{k}' \rangle \langle \mathbf{k}' | , \tag{2.23}$$

into equation (2.22). Since the resolution of the identity is equal to the identity element, inserting it into the expression has no effect on it's value. The vector states $|\mathbf{k}\rangle$ and $|\mathbf{k}'\rangle$ constitute a complete basis of free electron states and can therefore be described as virtual free particles. The insertion of resolution of the identity gives

$$S_{fi} = -i(2\pi)\delta(E_f - E_i) \int d^3x \int_{\mathbf{k}} \frac{d^3k}{(2\pi)^3} \int_{\mathbf{k}'} \frac{d^3k'}{(2\pi)^3} \langle e_2 | \mathbf{k}' \rangle \langle \mathbf{k}', \mathbf{p}' | \mathscr{H}_S(x) | \mathbf{k}, \mathbf{p} \rangle \langle \mathbf{k} | e_1 \rangle . \tag{2.24}$$

We can here identify $\langle e_2 | \mathbf{k}' \rangle = \sqrt{V} \psi_j^*(\mathbf{k}')$, the momentum space wave function of the electron in state j, and will use that evaluating notation henceforth. Let us now recall S_{fi} for the case of a free electron, i.e equation (2.9). By applying the same analytical steps as above on this expression, we get

$$S_{fi}^{free} = -i(2\pi)\delta(\tilde{E}_f - \tilde{E}_i) \langle \mathbf{p}', \mathbf{k}' | \int d^3x \mathscr{H}_s(x) | \mathbf{p}, \mathbf{k} \rangle . \tag{2.25}$$

Here, $\tilde{E}_i$ and $\tilde{E}_f$ denote the initial and final energy in the case of a free electron. It follows from the delta function that energy must be conserved for free electron scattering. We therefore define the scattering amplitude $\mathcal{M}(\mathbf{p}', \mathbf{k}', \mathbf{p}, \mathbf{k})$ for that case, in accordance with equation (2.9), as

$$S_{fi}^{free} = (2\pi)^4 \delta(\tilde{E}_f - \tilde{E}_i)\delta^3(\mathbf{p}' + \mathbf{k}' - \mathbf{p} - \mathbf{k}) \frac{\mathcal{M}(\mathbf{p}', \mathbf{k}', \mathbf{p}, \mathbf{k})}{4m_\chi m_e}. \tag{2.26}$$

Here, the mass-energy relation in the non-relativistic limit, i.e. $E = m$, has been applied. Comparing the two expressions for S_{fi}^{free} results in

$$\langle \mathbf{p}', \mathbf{k}' | \int d^3x \mathscr{H}_s(x) | \mathbf{p}, \mathbf{k} \rangle = i(2\pi)^3 \delta^3(\mathbf{p}' + \mathbf{k}' - \mathbf{p} - \mathbf{k}) \frac{\mathcal{M}(\mathbf{p}', \mathbf{k}', \mathbf{p}, \mathbf{k})}{4m_\chi m_e}. \tag{2.27}$$

We can once again introduce the momentum transfer $\mathbf{q} = \mathbf{p} - \mathbf{p}' = \mathbf{k}' - \mathbf{k}$. Since $\mathbf{p}' + \mathbf{k}' - \mathbf{p} - \mathbf{k} = \mathbf{k}' - \mathbf{k} - \mathbf{q}$, we can discard the $\mathbf{k}'$ integral in the expression for S_{fi} when we apply equation (2.27) onto (2.24). We then get

$$S_{fi} = (2\pi) V \delta(E_f - E_i) \int_{\mathbf{k}} \frac{d^3k}{(2\pi)^3} \psi_2^*(\mathbf{k} + \mathbf{q}) \frac{\mathcal{M}(\mathbf{p} - \mathbf{q}, \mathbf{k} + \mathbf{q}, \mathbf{p}, \mathbf{k})}{4m_\chi m_e} \psi_1(\mathbf{k}), \tag{2.28}$$

where ψ_1 and ψ_2 are the wave functions for a graphene valence electron before and after ejection. By reflecting on our starting point in equations (2.4), (2.5) and (2.7) we realise that $|S_{fi}|^2$ is of specfic interest and thus we want to square the absolute value of equation (2.28). Note that when $\delta(E_f - E_i)$ is squared a factor $T/(2\pi)$ is obtained. Thereby, $|S_{fi}|^2$ can be rewritten as

$$|S_{fi}|^2 = T(2\pi) V^2 \delta(E_f - E_i) \left| \int_{\mathbf{k}} \frac{d^3k}{(2\pi)^3} \psi_2^*(\mathbf{k} + \mathbf{q}) \frac{\mathcal{M}(\mathbf{p} - \mathbf{q}, \mathbf{k} + \mathbf{q}, \mathbf{p}, \mathbf{k})}{4m_\chi m_e} \psi_1(\mathbf{k}) \right|^2. \tag{2.29}$$

Finally, we can now calculate the differential rate of DM induced electron ejection by applying equation (2.29) to equation (2.7) according to

$$\begin{aligned} dR(\mathbf{q}) &= \frac{|S_{fi}(\mathbf{q})|^2}{TV^2} \frac{d^3q}{(2\pi)^3} = \\ &= \frac{d^3q}{T(2\pi)^3} T(2\pi) \delta(E_f - E_i) \left| \int_{\mathbf{k}} \frac{d^3k}{(2\pi)^3} \psi_2^*(\mathbf{k} + \mathbf{q}) \frac{\mathcal{M}(\mathbf{p} - \mathbf{q}, \mathbf{k} + \mathbf{q}, \mathbf{p}, \mathbf{k})}{4m_\chi m_e} \psi_1(\mathbf{k}) \right|^2 = \\ &= \delta(E_f - E_i) \frac{d^3q}{(2\pi)^2} \left| \int_{\mathbf{k}} \frac{d^3k}{(2\pi)^3} \psi_2^*(\mathbf{k} + \mathbf{q}) \frac{\mathcal{M}(\mathbf{p} - \mathbf{q}, \mathbf{k} + \mathbf{q}, \mathbf{p}, \mathbf{k})}{4m_\chi m_e} \psi_1(\mathbf{k}) \right|^2. \end{aligned} \tag{2.30}$$

By integrating over $\mathbf{q}$ and introducing the electron lattice momentum $\boldsymbol{\ell}$, we arrive at an expression for $v_{rel}\sigma(\boldsymbol{\ell}', \boldsymbol{\ell})$ as

$$v_{rel}\sigma(\boldsymbol{\ell}', \boldsymbol{\ell}) = \int_{\mathbf{q}} \frac{d^3q}{(2\pi)^2} \delta(E_f - E_i) \left| \int_{\mathbf{k}} \frac{d^3k}{(2\pi)^3} \psi_2^*(\boldsymbol{\ell}', \mathbf{k} + \mathbf{q}) \frac{\mathcal{M}(\mathbf{p} - \mathbf{q}, \mathbf{k} + \mathbf{q}, \mathbf{p}, \mathbf{k})}{4m_\chi m_e} \psi_1(\boldsymbol{\ell}, \mathbf{k}) \right|^2 \tag{2.31}$$

For reasons of linear independence, $\mathcal{M}(\mathbf{p}-\mathbf{q},\mathbf{k}+\mathbf{q},\mathbf{p},\mathbf{k}) = \mathcal{M}(\mathbf{q},\mathbf{v}_{\mathrm{el}}^{\perp})$. The vector $\mathbf{v}_{\mathrm{el}}^{\perp}$ is further defined in equation (2.40). What remains to be done is to introduce the definition of $\mathcal{M}$, in accordance with Hochberg et al. [20], as

$$\mathcal{M}(\mathbf{q},\mathbf{v}_{\mathrm{el}}^{\perp}) = \frac{4\sqrt{\pi}m_\chi m_e}{\mu_{e\chi}}\sqrt{\bar{\sigma}_e}F_{DM}(\mathbf{q},\mathbf{v}_{\mathrm{el}}^{\perp}), \tag{2.32}$$

where $\mu_{e\chi}$ is the reduced mass of a DM particle and an electron, and $\bar{\sigma}_e$ is a reference cross section. The form factor $F_{DM} = 1$ describes short range, or contact, interaction but will here be kept as a variable for the purpose of generalisation. If this is substituted into equation (2.31) we get

$$\begin{aligned} v_{rel}\sigma(\boldsymbol{\ell}',\boldsymbol{\ell}) = \frac{\bar{\sigma}_e\pi}{\mu_{e\chi}^2}\int_{\mathbf{q}}\frac{d^3q}{(2\pi)^2}\left|\int_{\mathbf{k}}\frac{d^3k}{(2\pi)^3}\psi_2^*(\boldsymbol{\ell}',\mathbf{k}+\mathbf{q})F_{DM}(\mathbf{q},\mathbf{v}_{\mathbf{el}}^{\perp})\psi_1(\boldsymbol{\ell},\mathbf{k})\right|^2 \\ \times\,\delta(E_f-E_i). \end{aligned} \tag{2.33}$$

The energy required to eject a valence electron is given by its binding energy $-E_i(\boldsymbol{\ell})$ and the work function Φ, which is the energy needed to escape from the Fermi level. The initial and final state energies, E_i and E_f, can therefore be expressed as,

$$\begin{aligned} E_i &= m_\chi + m_e + \frac{m_\chi}{2}v^2 + E_i(\boldsymbol{\ell}) + \Phi \\ E_f &= m_\chi + m_e + \frac{|m_\chi\mathbf{v}-\mathbf{q}|^2}{2m_\chi} + E_{er}, \end{aligned} \tag{2.34}$$

where E_{er} and $\frac{|m_\chi\mathbf{v}-\mathbf{q}|^2}{2m_\chi}$ are the kinetic energies of the electron and the DM particle, respectively, after ejection. $E_f - E_i$ can thus be expressed as $E_{er} + E_i(\boldsymbol{\ell}) + \Phi + \frac{q^2}{2m_\chi} - qv\cos\theta_{qv}$. For the sake of simplicity $E_f - E_i$ will be used as notation throughout most of this thesis. Equation (2.33) can now be specified further by noting that the wave function of the ejected, and thereby free, electron is well described by a plane wave in position space, i.e.

$$\psi_2^*(\mathbf{r}) = \frac{1}{\sqrt{V}}e^{-i\mathbf{k}_{\mathrm{f}}\cdot\mathbf{r}}. \tag{2.35}$$

By applying equation (2.35), we can now Fourier transform equation (2.33) from an integral over momentum $\mathbf{k}$ to an integral over space coordinates $\mathbf{r}$ and subsequently note that the space integral over $\mathbf{r}$ gives the Fourier transform of ψ_1 at $(\boldsymbol{\ell},\mathbf{q}-\mathbf{k}_{\mathrm{f}})$. This results in an expression for the cross section as

$$v_{rel}\sigma(\boldsymbol{\ell}) = \frac{\bar{\sigma}_e\pi}{\mu_{e\chi}^2}\int_{\mathbf{k}_{\mathrm{f}}}\frac{d^3k_{\mathrm{f}}}{(2\pi)^3}\int_{\mathbf{q}}\frac{d^3q}{(2\pi)^2}V\left|F_{DM}(\mathbf{q},\mathbf{v}_{\mathbf{el}}^{\perp})\right|^2\frac{\left|\widetilde{\psi}_1(\boldsymbol{\ell},\mathbf{q}-\mathbf{k}_{\mathrm{f}})\right|^2}{V}\times\delta(E_f-E_i). \tag{2.36}$$

This expression has been multiplied by $\frac{d^3\mathbf{k}_{\mathrm{f}}}{(2\pi)^3}V$ to account for the number of states with momentum around $\mathbf{k}_{\mathrm{f}}$. In doing this the V cancels out, resulting in

$$v_{rel}\sigma(\boldsymbol{\ell}) = \frac{\bar{\sigma}_e\pi}{\mu_{e\chi}^2}\int_{\mathbf{k}_{\mathrm{f}}}\frac{d^3k_{\mathrm{f}}}{(2\pi)^3}\int_{\mathbf{q}}\frac{d^3q}{(2\pi)^2}\left|F_{DM}(\mathbf{q},\mathbf{v}_{\mathbf{el}}^{\perp})\right|^2\left|\widetilde{\psi}_1(\boldsymbol{\ell},\mathbf{q}-\mathbf{k}_{\mathrm{f}})\right|^2\times\delta(E_f-E_i). \tag{2.37}$$

Since the outgoing electron has no lattice momentum, we omit the variable $\boldsymbol{\ell}'$ from the expression. Equation (2.37) is equivalent to equation (5) in the correlative article by Hochberg et al. [20], which was discussed in section 1.2.3. We can now sum over the four valence electrons and account for the spin degeneracy of each band, and finally get

$$R = 2 \sum_{i=\pi,\sigma_1,\sigma_2,\sigma_3} \frac{\rho_\chi}{m_\chi} N_C A_{uc} \int_{1\mathrm{BZ}} \frac{d^2\ell}{(2\pi)^2} \int_{\mathbf{v}} d^3v g(\mathbf{v}) v_{\mathrm{rel}} \sigma_i(\boldsymbol{\ell}). \tag{2.38}$$

The DM velocity distribution $g(\mathbf{v})$ is measured in the laboratory frame, a more detailed description of which can be found in Appendix A.1. Furthermore, $\rho_\chi = 0.4$ GeV/cm^3 is the local galaxy DM density, $m_\chi = 100$ MeV is the mass of a DM particle used in all calculations of this thesis, and $N_C = 5 \cdot 10^{25}$ kg^{-1} is the atomic density of graphene. $A_{uc} = 3\sqrt{(3)}a^2/2$ is the area of the unit cell of graphene, i.e a hexagonal and two-dimensional cell with carbon-carbon bond length $a = 1.42$ Å. All values of known physical quantities have been set in accordance with Hochberg et al. [20] and [23].

2.1.3 Modification of the Scattering Amplitude

Up until this point we have, in accordance with Hochberg et al. [20], assumed that the scattering amplitude $\mathcal{M}$ does not depend on the momentum transfer $\mathbf{q}$, apart from the $\mathbf{q}$ dependence in the general form factor $F_{DM}(\mathbf{q}, \mathbf{v}_{\mathbf{el}}^{\perp})$. Equation (2.37) can however be generalised in terms of a squared spin-averaged electron ejection amplitude $\overline{|\mathcal{M}_{1\to2}|^2}$, the definition of which is presented in equation (2.41) [24]. Using this, equation (2.37) can be rewritten as

$$v_{rel}\sigma = \frac{1}{16 m_\chi^2 m_e^2} \int_{\mathbf{q}} \frac{d^3q}{(2\pi)^3} \overline{|\mathcal{M}_{1\to2}|^2} 2\pi \times \delta(E_f - E_i). \tag{2.39}$$

For $\overline{|\mathcal{M}_{1\to2}|^2}$ to be physically realistic a few conditions apply. First of all, it should be invariant under spacial translation and three dimensional rotation. Furthermore, invariance under Galilean transformation, i.e. a coordinate transformation between reference frames differing by constant relative motion, is required. Assuming these restrictions, $\overline{|\mathcal{M}_{1\to2}|^2}$ can be composed out of 14 different combinations of $\mathbf{q}$, $\mathbf{v}_{\mathrm{el}}^{\perp}$, $\mathbf{S}_\chi$ and $\mathbf{S}_e$, which can be seen in Table I in [24]. Here, $\mathbf{S}_\chi$ and $\mathbf{S}_e$ are the electron and DM particle spin operators and $\mathbf{v}_{\mathrm{el}}^{\perp}$ is defined as

$$\mathbf{v}_{\mathrm{el}}^{\perp} = \mathbf{v} - \frac{\mathbf{q}}{2\mu_{e\chi}} - \frac{\mathbf{k}}{2m_e}. \tag{2.40}$$

Note that $\mathbf{v}_{\mathrm{el}}^{\perp}$ is only introduced for the sake of analytical derivation and will not be regarded in any numerical evaluation. In [24] the interaction between DM particles and atomically bound electrons is regarded, and thus the expression for the spin averaged transition amplitude for the electron with quantum numbers nl is given as

$$\overline{\left|\mathcal{M}_{1\to2}^{nl}\right|^2} = \sum_{i=1}^{4} R_i^{nl}\left(\mathbf{v}_{\mathrm{el}}^{\perp}, \frac{\mathbf{q}}{m_e}\right) W_i^{nl}(k', \mathbf{q}). \tag{2.41}$$

We, however, are studying electrons bound in graphene, which reside in the four energy bands π, σ_1, σ_2 and σ_3. Instead of the quantum numbers n and l, our amplitudes are given for these bands. The DM response functions R_i^{nl} will nonetheless remain unchanged regardless of how the electrons are bound. The first response function R_1^{nl} is given as

$$R_1^{nl}\left(\mathbf{v}_{\text{el}}^{\perp}, \frac{\mathbf{q}}{m_e}\right) \equiv c_1^2 + \frac{c_3^2}{4}\left(\frac{\mathbf{q}}{m_e}\right)^2\left(\mathbf{v}_{\text{el}}^{\perp}\right)^2 - \frac{c_3^2}{4}\left(\frac{\mathbf{q}}{m_e}\cdot\mathbf{v}_{\text{el}}^{\perp}\right)^2 + \frac{c_7^2}{4}\left(\mathbf{v}_{\text{el}}^{\perp}\right)^2 + \frac{c_{10}^2}{4}\left(\frac{\mathbf{q}}{m_e}\right)^2 +$$
$$+ \frac{j_\chi(j_\chi+1)}{12}\Bigg\{3c_4^2c_6^2\left(\frac{\mathbf{q}}{m_e}\right)^4 + \left(4c_8^2+2c_{12}^2\right)\left(\mathbf{v}_{\text{el}}^{\perp}\right)^2 + \left(2c_9^2+4c_{11}^2+2c_4c_6\right)\left(\frac{\mathbf{q}}{m_e}\right)^2 +$$
$$+ \left(4c_5^2+c_{13}^2+c_{14}^2-2c_{12}c_{15}\right)\left(\frac{\mathbf{q}}{m_e}\right)^2\left(\mathbf{v}_{\text{el}}^{\perp}\right)^2 + c_{15}^2\left(\frac{\mathbf{q}}{m_e}\right)^4\left(\mathbf{v}_{\text{el}}^{\perp}\right)^2 -$$
$$- c_{15}^2\left(\frac{\mathbf{q}}{m_e}\right)^2\left(\mathbf{v}_{\text{el}}^{\perp}\cdot\frac{\mathbf{q}}{m_e}\right)^2 + \left(-4c_5^2+2c_{13}c_{14}+2c_{12}c_{15}\right)\left(\mathbf{v}_{\text{el}}^{\perp}\cdot\frac{\mathbf{q}}{m_e}\right)^2\Bigg\}, \tag{2.42}$$

where c_i, $i = 1, ..., 15$, are coefficients. Here, the original relation between $\mathcal{M}$ and $\mathbf{q}$, as assumed in section 2.1.2, corresponds to $c_i = 0$ for $i > 1$. As mentioned, due to time limitation and numerical unfeasibility within the scope of this thesis, only terms where the scattering amplitude is independent of $\mathbf{v}_{\text{el}}^{\perp}$, i.e. $\overline{|\mathcal{M}_{1\to2}(\mathbf{q}))|^2} \propto \mathbf{q}^2$ and $\overline{|\mathcal{M}_{1\to2}(\mathbf{q}))|^2} \propto \mathbf{q}^2$, will be studied. For physical context, these scattering amplitudes are expected in models where DM particles are regarded as fermions and interact with electrons via the exchange of pseudo-scalar particles, or in models where DM has spin 0 and interactions violate parity and charge conjugation parity.

Since we are only interested in events in which an electron is ejected, and the wave functions are spin-independent, our analogue of the first atomic response function $W_1^{nl}(k', \mathbf{q})$ is given as

$$W_1^j(\boldsymbol{\ell}, \mathbf{k}_{\text{f}}, \mathbf{q}) = \left|\widetilde{\psi}_j(\boldsymbol{\ell}, \mathbf{q}-\mathbf{k}_{\text{f}})\right|^2. \tag{2.43}$$

where j corresponds to the different energy bands. Here the same operation as in the derivation of equation (2.36) was used to evaluate the integral over $\mathbf{k}$ by noting that the integral is the Fourier transform of the initial electron wave function $\psi_j(\mathbf{r})$ evaluated at $\mathbf{q}-\mathbf{k}_{\text{f}}$. The expression for the first term of $|\mathcal{M}_{1\to2}|^2$, i.e. equation (2.41), can now be substituted into equation (2.39), integrating over the final electron momentum $\mathbf{k_f}$ and yielding

$$v_{rel}\sigma_j(\boldsymbol{\ell}) = \frac{1}{16m_\chi^2m_e^2}\int_{\mathbf{k}_{\text{f}}}\frac{d^3k_{\text{f}}}{(2\pi)^3}\int_{\mathbf{q}}\frac{d^3q}{(2\pi)^3}R_1^j\left(\mathbf{v}_{el}^{\perp}, \frac{\mathbf{q}}{m_e}\right)\left|\tilde{\psi}_j(\boldsymbol{\ell}, \mathbf{q}-\mathbf{k}_{\text{f}})\right|^2 \times 2\pi\delta(E_f - E_i). \tag{2.44}$$

By comparing this expression with equation (2.37) we see that the difference is an overall factor and the replacement of $|F_{DM}|^2$ with R_1^j.

3

Computation of the Ejection Rate

The following sections describe the numerical evaluation of the analytically derived DM induced electron ejection rate, both before and after the modification of the scattering amplitude $\mathcal{M}$, as described in section 2.1.3.

3.1 Recasting the Ejection Rate for Numerical Evaluation

In order to enable and facilitate the numerical evaluation of the DM induced ejection rate, the derived expression can be reformulated. Furthermore, the eigenvectors and band energies of the pertinent wave functions can be calculated and tabulated prior to the final computation. These steps are described in the following sections.

3.1.1 Analytical Manipulations

To aid the numerical integration, a number of algebraic and analytical manipulations can be performed. As has been discussed, since only short range interactions are of interest, we let

$$F_{DM}(\mathbf{q}, \mathbf{v}_{\mathrm{el}}^{\perp}) = 1, \tag{3.1}$$

in accordance with [24]. Note that the following derivation is valid only when F_{DM} is independent of $\mathbf{v}_{\mathrm{el}}^{\perp}$. To emphasise this, the notation $F_{DM}(\mathbf{q})$ for the form factor will be used henceforth. With that in mind, the volume integral over $\mathbf{v}$ can be rewritten in spherical coordinates projected onto the direction of $\mathbf{q}$ according to

$$\int d^3v = \int dv v^2 \int_0^{2\pi} d\phi \int_{-1}^{1} d\cos\theta_{qv}. \tag{3.2}$$

Using this formulation, as is described in detail in Appendix A.2, the ejection rate can be rewritten as

$$\frac{dR}{d\ln(E_{er})} = 2 \sum_{i=\pi,\sigma_1,\sigma_2,\sigma_3} \frac{\rho_\chi}{m_\chi} N_c A_{uc} \frac{\bar{\sigma}_e}{\mu_{e\chi}^2} \int_{1\mathrm{BZ}} \frac{d^2\ell}{(2\pi)^2} \int \frac{d\Omega_{k_\mathrm{f}}}{(2\pi)^3} \frac{k_\mathrm{f}^3}{2} \int_{q_{\min}}^{q_{\max}} \frac{d^3q}{4\pi} \frac{\pi}{q} \eta(v_{\min}) \times \left|F_{DM}(\mathbf{q})\right|^2 \left|\tilde{\psi}_i(\boldsymbol{\ell}, \mathbf{q} - \mathbf{k}_\mathrm{f})\right|^2, \tag{3.3}$$

where $\eta(v_{\min})$ is defined as

$$\eta(v_{\min}) = \int d\Omega_{qv} \int\limits_{v>v_{\min}} dv \cdot vg(v). \tag{3.4}$$

Under the assumption that the DM velocity distribution, $g(v)$, takes the form of a Maxwell-Boltzmann distribution with an upper limit at the galactic escape velocity, in accordance with [24], $\eta(v_{\min})$ can by evaluated analytically. These calculations are performed in Appendix A.3, and result in

$$\begin{aligned}
\eta_1(v_{\min}) &= \frac{v_0^2\pi}{2v_\oplus N_\eta}\Big(- 4e^{-v_{esc}^2/{v_0}^2}v_\oplus + \sqrt{\pi}v_0\Big[\operatorname{erf}\left(\frac{v_{\min}+v_\oplus}{v_0}\right) - \operatorname{erf}\left(\frac{v_{\min}-v_E}{v_0}\right)\Big]\Big) \\
\eta_2(v_{\min}) &= \frac{v_0^2\pi}{2v_\oplus N_\eta}\Big(- 2e^{-v_{esc}^2/{v_0}^2}(v_{esc}-v_{\min}+v_\oplus) + \sqrt{\pi}v_0\Big[\operatorname{erf}\left(\frac{v_{esc}}{v_0}\right) - \\
&\qquad \operatorname{erf}\left(\frac{v_{\min}-v_\oplus}{v_0}\right)\Big]\Big),
\end{aligned} \tag{3.5}$$

where $\eta_1(v_{\min})$ and $\eta_2(v_{\min})$ correspond to $v_{\min} < v_{\text{esc}} - v_\oplus$ and $v_{\min} > v_{\text{esc}} - v_\oplus$, respectively. Moreover, erf is the Gauss error function, which is a non-elementary function defined as

$$\operatorname{erf}(x) = \frac{1}{\sqrt{\pi}}\int_{-x}^{x} e^{-t^2}dt = \frac{2}{\sqrt{\pi}}\int_0^x e^{-t^2}dt. \tag{3.6}$$

The normalisation constant N_η is given as

$$N_\eta = v_0^3\pi\left[\operatorname{erf}\left(\frac{v_{esc}}{v_0}\right) - 2\frac{v_{esc}}{v_0}\exp\left[-\left(\frac{v_{esc}}{v_0}\right)^2\right]\right]. \tag{3.7}$$

This reformulated and somewhat simplified expression for the ejection rate, given in equation (3.3), streamlines the numerical evaluation and eliminates the delta function. The specifics of $v_{\max}$ and $v_{\min}$, as well as the velocity distribution $g(v)$, are presented in Appendix A.1.

3.1.2 Calculations of the Wave Function Parameters

Once the described reformulations have been applied the only remaining components of the ejection rate that need to be specified are the wave functions of the graphene valence electrons. As has been discussed, these electrons appear in four different bands: π, σ_1, σ_2 and σ_3. The normalisation of the π band can be calculated analytically and expressed as

$$\widetilde{N_\pi}(\boldsymbol{\ell}) = \sqrt{\frac{(2\pi)^3}{1 + s\sum_{j=1}^{3}\cos(\varphi_\ell + \mathbf{r}\cdot\mathbf{R}_j)}} \tag{3.8}$$

by assuming a tight-binding model. Here, $\varphi_\ell = -\arctan(\operatorname{Im}(f(\boldsymbol{\ell}))/\operatorname{Re}(f(\boldsymbol{\ell})))$ describes the angles of the phase factor $f(\boldsymbol{\ell}) = e^{i\boldsymbol{\ell}\cdot\mathbf{R}_1} + e^{i\boldsymbol{\ell}\cdot\mathbf{R}_2} + e^{i\boldsymbol{\ell}\cdot\mathbf{R}_3}$ and the overlap,

s, between the atomic orbitals is set to $s = 0.129$, in accordance with [26]. However, in momentum space the phase factor picks up an extra momentum term as $f(\boldsymbol{\ell}+\mathbf{k})$. For further detail see appendix B.1.3. The band energy for the different bands, $E_{\text{band}}(\boldsymbol{\ell})$, can be calculated by solving for the different energy eigenvalues in

$$\det|\mathcal{H} - E_{\text{band}}(\boldsymbol{\ell})\mathcal{S}| = 0. \tag{3.9}$$

The overlapping integral matrix, $\mathcal{S}$, and the transfer integral matrix, $\mathcal{H}$, for the π band are defined as

$$\mathcal{S} = \begin{pmatrix} 1 & sf(\boldsymbol{\ell}) \\ sf(\boldsymbol{\ell})^* & 1 \end{pmatrix}, \quad \mathcal{H} = \begin{pmatrix} \epsilon_{2p} & tf(\boldsymbol{\ell}) \\ tf(\boldsymbol{\ell})^* & \epsilon_{2p} \end{pmatrix}, \tag{3.10}$$

where $s = 0.129$ is the overlap integral and $t = -3.03\,\text{eV}$ is the transfer integral between nearest neighbours. Moreover, $\epsilon_{2s} = -8.87$ eV is given relative to ϵ_{2p} and hence $\epsilon_{2p} = 0$ is chosen for the sake of simplicity [20]. The calculation of the π band energy, which is performed in detail in Appendix B.1.2, results in

$$E_\pi(\ell) = \frac{\epsilon_{2p} \pm t|f(\boldsymbol{\ell})|}{1 \pm s|f(\boldsymbol{\ell})|}. \tag{3.11}$$

Note that only the negative solution, corresponding to the valence band, is necessary for the purpose of this thesis. The valence energy band for π is plotted in Figure B.2.

The normalisation of the σ_i wave functions can similarly be performed under the assumption of a tight-binding model, evaluated in Euclidean space. Thus, $\langle\psi_{\sigma_i}|\psi_{\sigma_i}\rangle$ should be evaluated over its closest neighbours, where

$$\psi_{\sigma_i} = \mathbf{C}_i \begin{bmatrix} \phi_{2s}(\mathbf{r}) \\ \phi_{2p_x}(\mathbf{r}) \\ \phi_{2p_y}(\mathbf{r}) \\ \frac{1}{\sqrt{3}}\sum_j \phi_{2s}(\mathbf{r}-\mathbf{R}_j)e^{i\boldsymbol{\ell}\cdot\mathbf{R}_j} \\ \frac{1}{\sqrt{3}}\sum_j \phi_{2p_x}(\mathbf{r}-\mathbf{R}_j)e^{i\boldsymbol{\ell}\cdot\mathbf{R}_j} \\ \frac{1}{\sqrt{3}}\sum_j \phi_{2p_y}(\mathbf{r}-\mathbf{R}_j)e^{i\boldsymbol{\ell}\cdot\mathbf{R}_j} \end{bmatrix}. \tag{3.12}$$

$\mathbf{C}_i$ is the eigenvector derived from solving equation (3.9) for each respective energy band, see figure B.2. Note that the band energies are plotted for $-E_i(\boldsymbol{\ell})$. These calculations are described in detail in Appendix B.1. From the tight-binding model the overlap $\langle\phi(\mathbf{r}-\mathbf{R}_i)|\phi(\mathbf{r}-\mathbf{R}_j)\rangle = 0$ for $i \neq j$ and all atomic wavefunctions $\phi(\mathbf{r})$, resulting in $N_\sigma(\boldsymbol{\ell}) = \sqrt{(2\pi)^3/n_\sigma(\boldsymbol{\ell})}$, where $n_\sigma(\boldsymbol{\ell})$ is given as

$$\begin{aligned} n_\sigma(\boldsymbol{\ell}) =& C_1^*C_1 + C_2^*C_2 + C_3^*C_3 + 3(C_4^*C_4 + C_5^*C_5 + C_6^*C_6) \\ & 2\,\text{Re}\Big[S_{\text{ss}}C_1^*C_4 + S_{\text{sp}}C_1^*C_5 + S_{\text{sp}}C_1^*C_6 + S_{\text{sp}}C_2^*C_3 + S_\sigma C_2^*C_5 + \\ & S_\pi C_2^*C_6 + S_{\text{sp}}C_3^*C_4 + S_\pi C_3^*C_5 + S_\sigma C_3^*C_6 \sum_{j=1}^{3} e^{i\boldsymbol{\ell}\cdot\mathbf{R}_j}\Big]. \end{aligned} \tag{3.13}$$

The overlap parameters, S_{ss}, S_{sp}, S_σ and S_π, are specified in Table B.1. The band energy can be found for each σ by solving for the energy eigenvalues in equation

(3.9). In the case of the σ bands, $\mathcal{S}$ and $\mathcal{H}$ are 6×6 matrices, derived from the 3×3 submatrices given in Appendix B.1.2. Note again that only the negative solutions, corresponding to the valence bands, are of interest in this thesis. Due to the complexity of this calculation, the eigenvalues and the band energies require numerical evaluation and tabulation for each respective σ band over a reciprocal grid in the first Brillouin zone.

3.2 Numerical Evaluation of the Ejection Rate

It is important to note that although all analytical derivations, most notably in Chapter 2, have assumed natural units, all physical quantities have been expressed in SI units. For the sake of continuity, all computations have been performed using SI units. This conversion of units entails a division by a factor of $\hbar$ for each of the momenta $\mathbf{k}_\mathrm{f}$ and $\mathbf{q}$, in order to achieve the correct dimensions.

While all preparatory calculations of the σ eigenvectors and their band energies were tabulated using *Wolfram Mathematica*, the evaluation of the DM induced electron ejection rate was performed using *Python* and is publicly available at [27]. After the preambulatory reformulation of equation (2.39) to the more computable form seen in equation (3.3), the differential rate was evaluated for each band separately. The differential ejection rate depends on a multidimensional integral accordning to

$$\int_{1BZ} d^2\ell \int_{\partial\Omega_{k_\mathrm{f}}} d\Omega_{k_\mathrm{f}} k_\mathrm{f}^3 \int_{q_\mathrm{min}}^{q_\mathrm{max}} \frac{d^3q}{q} \eta(v_\mathrm{min}) \times |F_{DM}(\mathbf{q})|^2 \left|\tilde{\psi}_i(\boldsymbol{\ell}, \mathbf{q} - \mathbf{k}_\mathrm{f})\right|^2 . \tag{3.14}$$

Due to the complexity of the calculations, the code was run in parallel over the cores of the computer. In each thread, every value of $\mathbf{k}_\mathrm{f}$ was regarded in a loop and a lambda function of the lattice vector $\boldsymbol{\ell}$ was created. This enabled the utilisation of Gauss-Legendre quadrature, defined by the library *mpmath*. This lambda function was then integrated over the differential angle Ω_{k_f}. Each such integration contained an additional integration over momentum space $\mathbf{q}$, which relates to v through the delta function such that $v_\mathrm{min} = \frac{E_{er}+E_i(\boldsymbol{\ell})+\Phi}{q} + \frac{q}{2m_\chi}$. This integral was performed with integration limits as specified in Appendix A.4. In equation (3.14), the two inner integrals were evaluated on a 17×17 grid over the first Brillouin zone. All points were then multiplied by its discretised differential area $d^2\ell$ and subsequently summed over, thus approximating the last integral over the lattice momentum in the first Brillouin zone. This yielded the final numerical evaluation of equation (3.3) for a given $\mathbf{k}_\mathrm{f}$ and thereby the values of the ejection rate could be plotted as a function of $E_{er} = k_\mathrm{f}^2/2m_e$.

3.3 Implementation of the Modified Scattering Amplitudes

The implementation of the additional interaction cases was, for the leading response function $R_1^j\left(\mathbf{v}_{\text{el}}^{\perp}, \frac{\mathbf{q}}{m_e}\right)$, simply a matter of replacing the previous DM form factor, given in equation (2.44). Note again that due to the additional $\mathbf{v}$ and $\mathbf{q}$ dependence, the analytical evaluation of $\eta(v_{\min})$ was no longer possible. Furthermore, this lead to a significant increase in computation time, a discussion of which is presented in section 5.2. As has been explained, a result of this is the limitation to contributions from terms solely dependent on $\mathbf{q}$, i.e. $\overline{|\mathcal{M}_{1\to 2}|^2} \propto |\mathbf{q}|^2$ and $\overline{|\mathcal{M}_{1\to 2}|^2} \propto |\mathbf{q}|^4$. These modifications are achieved by redefining the form factor F_{DM} as

$$F_{DM}(\mathbf{q}) = A_1 |\mathbf{q}| \qquad \text{and} \qquad F_{DM}(\mathbf{q}) = A_2 |\mathbf{q}|^2, \tag{3.15}$$

for each respective case. Here, the coupling constants A_1 and A_2 govern the strength of the interactions and are modifications of $\bar{\sigma}_e$ in equation (2.32). These constants only contribute a multiplicative factor to the whole expression and does not influence the qualitative behaviour. Thus they are parameters to the model and have in this thesis, where applicable, been set to align the starting points of the ejection rates with different F_{DM}, to allow for clearer comparison of the qualitative behaviour.

4

Numerical Results

In this chapter, all computed ejection rates are presented. Initially, the case of a scattering amplitude independent of the momentum transfer, which has previously been studied by Hochberg et al. [20], is shown. This will allow for the comparison of the obtained results with previous findings. Secondly, the ejection rates for each of the described scattering amplitudes are presented as well.

4.1 Ejection Rate for a Constant Scattering Amplitude

As has been explained, the DM induced electron ejection rate has previously been computed for $|\mathcal{M}|^2 \propto 1$ by Hochberg et al. [20]. However, there seems to be an inconsistency in the normalisation of the wave functions in their article, which will be discussed in more detail in section 5.1. For the sake of comparison, this case has thus been computed both with and without the correction of this normalisation. The corresponding ejection rates can be seen in Figure 4.1. Note that the corrected normalisation has been used for all other computations.

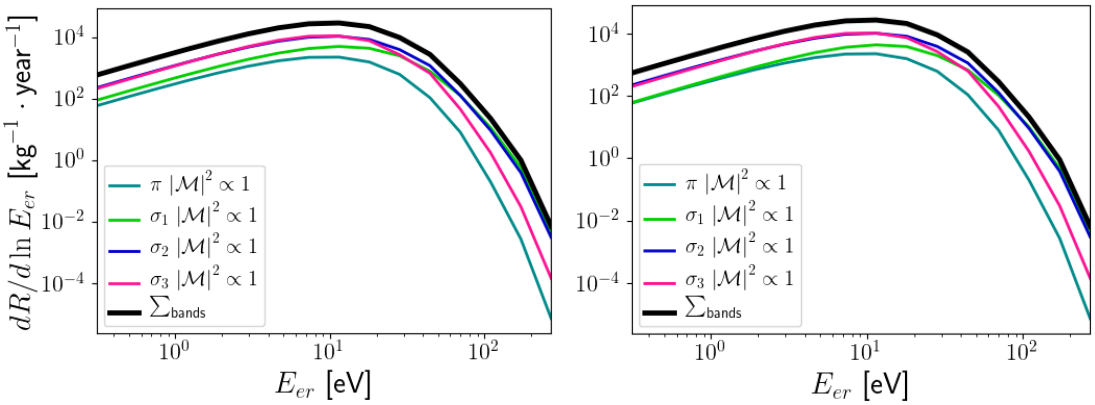

(a) With corrected normalisation **(b)** Without corrected normalisation

Figure 4.1: The differential ejection rates for an incoming DM particle with m_χ=100 MeV, $\bar{\sigma}_e = 10^{-37}\text{cm}^2$ and $F_{DM} = 1$, shown for each valence band as well as their joint contribution. The corrected normalisation has been applied to (a) while it has been omitted in (b). The differential rate is plotted in units of ejected electrons per kg of graphene and year, as a function of kinetic energy of the ejected electrons, E_{er}. Note that σ_1 and σ_2 dominate at higher electron ejection energies.

Here it is apparent that correcting the normalisation yields only a slight difference. This dissimilarity is most visible at the starting point of the rates, where the σ_1 and π bands coincide without the implementation of the correction while they separate with this implementation. In both cases, the same quantitative behaviour is apparent, including the higher contribution of σ_1 and σ_2 to the total rate for large electron ejection energies.

4.2 Ejection Rates for the Modified Scattering Amplitudes

In addition to comparing the case of $|\mathcal{M}|^2 \propto 1$ to previously published work, this case was also compared to the ejection rates given for $|\mathcal{M}|^2 \propto |\mathbf{q}|^2$ and $|\mathcal{M}|^2 \propto |\mathbf{q}|^4$. These three cases are plotted for each respective valence band in Figure 4.2.

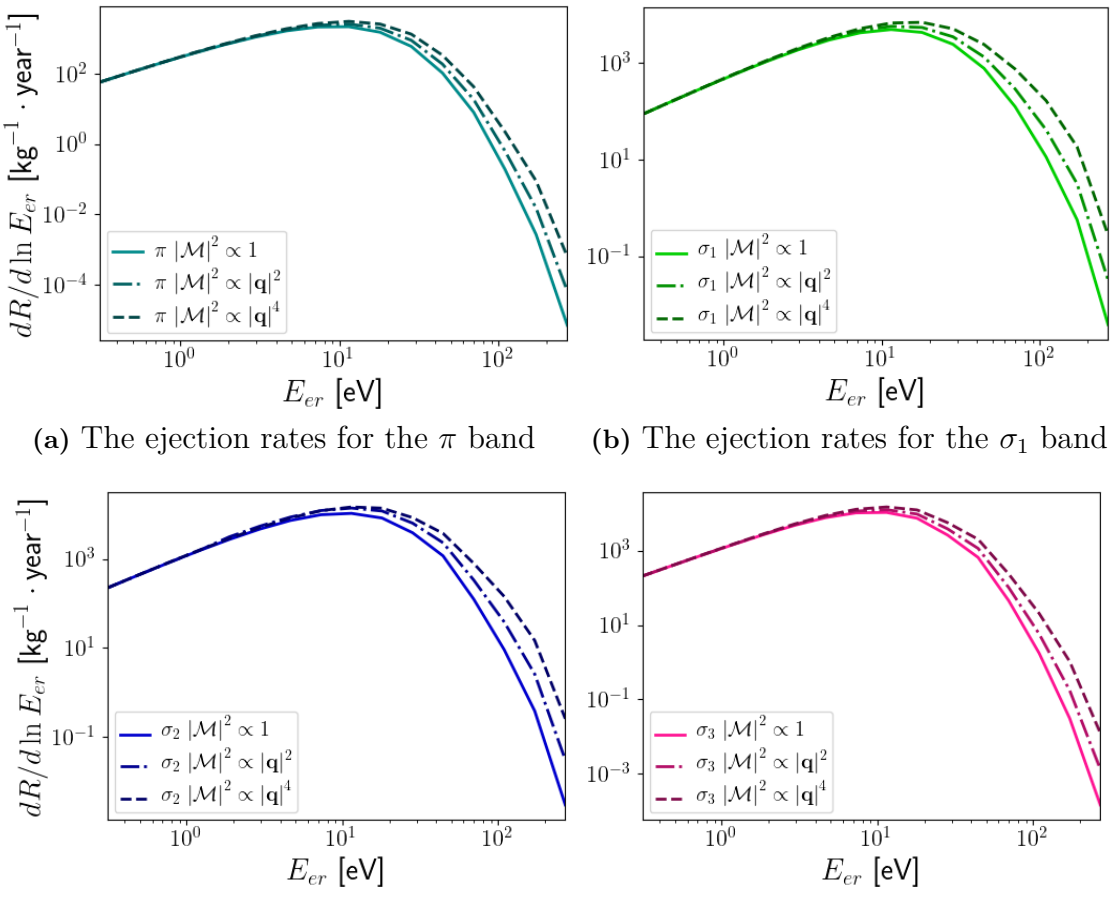

(a) The ejection rates for the π band **(b)** The ejection rates for the σ_1 band

(c) The ejection rates for the σ_2 band **(d)** The ejection rates for the σ_3 band

Figure 4.2: The differential ejection rate for an incoming DM particle with m_χ=100 MeV and $\bar{\sigma}_e = 10^{-37}\text{cm}^2$, for each scattering amplitude. The rates are given for every valence band respectively and are plotted in units of ejected electrons per kg of graphene and year, as a function of kinetic energy of the ejected electrons, E_{er}. It can here be seen that the rate decreases less rapidly for $|\mathbf{q}|$ of higher powers.

By studying Figure 4.2, it is apparent that initially there is little to no difference between the different scattering amplitudes. As the energy E_{er} increases, however, some dissimilarities appear. For each valence band, it is clear that the differential ejection rate decreases less rapidly for $|\mathcal{M}|^2 \propto |\mathbf{q}|^2$ and even less so for $|\mathcal{M}|^2 \propto |\mathbf{q}|^4$. Moreover, the ejection rate reaches its peak for a slightly higher kinetic energy E_{er} as the scattering amplitude is proportional to $|\mathbf{q}|$ of a higher power. This difference is, however, minor. The identified differences are reaffirmed by studying the total ejection rate of each scattering amplitude, as shown in Figure 4.3.

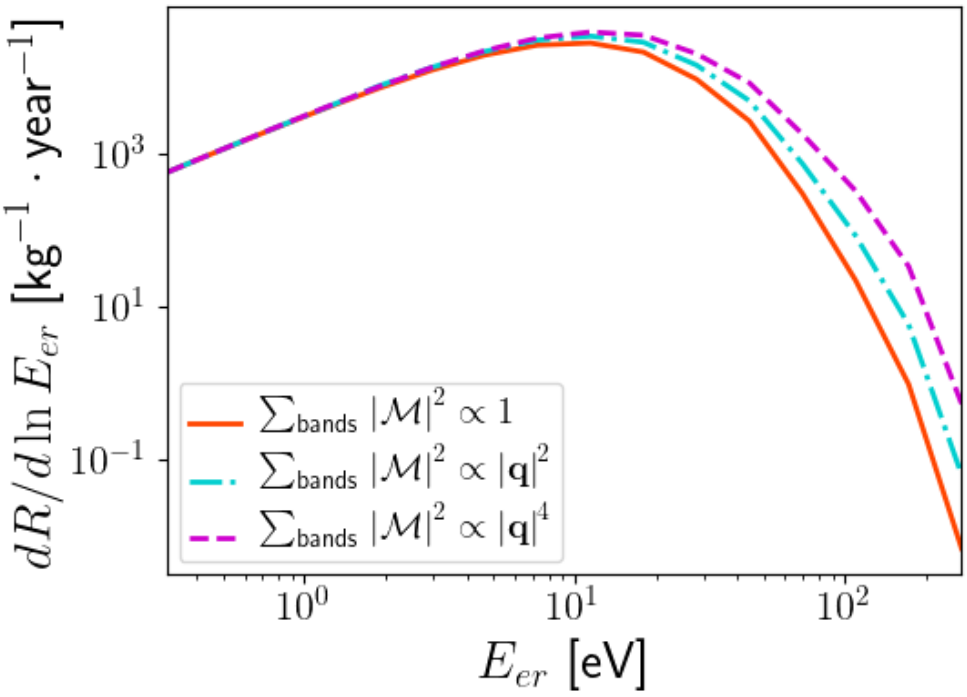

Figure 4.3: The total differential ejection rate for an incoming DM particle with m_χ=100 MeV and $\bar{\sigma}_e = 10^{-37}\text{cm}^2$, for each scattering amplitude. The rates are plotted in units of ejected electrons per kg of graphene and year, as a function of kinetic energy of the ejected electrons E_{er}. Once again it is apparent that the rate decreases less rapidly for $|\mathbf{q}|$ of higher powers.

Here, it is once again clear that while the difference is slight, there is a clear distinction in the rapidity of decline of the ejection rate for each scattering amplitude.

5
Conclusions

This chapter aims to discuss the computed ejection rates, both in relation to previously published results and comparatively for the different scattering amplitudes. Furthermore, the computational challenges and the multiple strategies to aid these are discussed as well. Lastly, some possibilities of further research are presented.

5.1 Comparison of the Ejection Rates

In the following sections the calculated DM induced electron ejection rates are compared for different cases. Initially, the corresponding results are compared to those achieved by Hochberg et al. [20]. Thereafter, the ejection rates for each of the specified scattering amplitudes are compared.

5.1.1 Comparison with Previous Published Results

Since the ejection rate for $|\mathcal{M}|^2 \propto 1$ has previously been computed by Hochberg et al. [20] their results can be compared with those generated within this thesis. As has already been noted, the wave function, specifically the Bloch function Φ_B described in equation (B.2), was not correctly normalised by Hochberg et al. [20]. As presented in Appendix B.1, a factor of $1/\sqrt{3}$ arises since Φ_B is a sum over the three nearest atomic neighbours. However, the general Bloch wave function in Hochberg et al. [20], defined in (B.1), is correctly normalised. Since Hochberg et al. [20] have not published any code nor primary data, it is not possible to determine what normalisation was used to obtain the results of their article. At the very least, the theory around the Bloch normalisation in Hochberg et al. [20] is misleading and possibly somewhat incorrect. This discrepancy may be the origin of some differences between the results generated by Hochberg et al. [20] and those of this thesis. However, as is clear in Figure 4.1, correcting this normalisation yields only a slight change of the ejection rate.

By comparing Figure 4.1 with Figure 1 in [20], it is clear that their results differ from the results presented here, even when the normalisation is performed by their specifications. Most noticeable is that the relative sizes of the ejection rates for each band in Figure from Hochberg et al. 4.1 do not correspond to the results of Hochberg et al. [20]. Moreover, the relative contribution from each valence band does not directly correspond to the ordering of the binding energies given from least to most bound as $\pi, \sigma_3, \sigma_2, \sigma_1$, seen in Figure B.2. This contradicts the presumption

that the π electron should have the greatest ejection rate for low electron ejection energies since it is the most loosely bound band. However, since the energy contributes to both the limits on $\mathbf{q}$ and $v_{\min}$, this discrepancy entails more than a simple scalar correction. The qualitative properties of each band does, however, conform for the different results. For instance, in Figure 4.1 σ_1 and σ_2 can be seen to have the greatest contribution at large electron ejection energies. This observation is physically realistic since σ_1 and σ_2 are 2s dominated and will thus have a larger spread in momentum, and will thereby contribute more for higher kinetic energies of the ejected electrons. Overall, this comparison suggests that the computations differ only slightly between this thesis and Hochberg et al. [20].

5.1.2 Impact of Different Scattering Amplitudes

By comparing the ejection rates for each of the specified cases, i.e. $|\mathcal{M}|^2 \propto 1$, $|\mathcal{M}|^2 \propto |\mathbf{q}|^2$ and $|\mathcal{M}|^2 \propto |\mathbf{q}|^4$, a few clear differences can be seen. First of all, it is important to note that the magnitudes of the rates are somewhat arbitrary, since $\bar{\sigma}_e$ and A_i, $i = 1, 2$, as defined in (3.15), are unknown model parameters. Note that the relative sizes of the different valence bands within the same case should nonetheless remain, as these are determined by the same parameters. In order to specify these factors, the models have to be fitted to any future experimental data, possibly from the PTOLEMY detector, with regard to their magnitudes. This ambiguity entails a greater emphasis on the qualitative properties of the ejection rates. As has been described, the main differences between the cases are the decrease of ejection rate as the electron energy increases and, to a lesser degree, the kinetic energy needed for the maximum ejection rate. More precisely, it has been seen that as the scattering amplitude is proportional to $|\mathbf{q}|$ of a higher power, the decline lessens in rapidity. This property is expected since the momentum transfer $|\mathbf{q}|$ increases with increasing electron energy and as the power of $|\mathbf{q}|$ increases, the scattering amplitude is more dominantly dependent on this quantity.

The implementation of a momentum transfer dependence in the scattering amplitude under the use of graphene as target material for direct detection of DM has not previously been considered. The calculations in this thesis are thus unique and extend the calculations performed by Hochberg et al. [20]. Thereby the number of theoretical models with which future experimental data can be compared has been extended. This thesis is therefore directly contributing to current research within detection of DM which will hopefully yield groundbreaking results in the near future.

5.2 Computational Challenges

Throughout the course of this project, computational limits constituted a crucial and persisting restriction. Even in the simplest case, with F_{DM} set to 1, the combined calculations were on the verge of the limit of feasibility with the available computers. A number of different computational methods were attempted in order to speed up the calculations, the most notable of which are described here. In spite of countless attempted variations of the method, the calculations remained a com-

putational challenge.

The initial approach to the computational difficulties was an evaluation of the performance of different libraries for computing integrals in *Python*. After benchmarking, it was found that *mpmath* gave the best results with regard to computation speed, and thus it was subsequently used in the code. Another approach, though not fully explored, was changing the implementation language to one with shorter compilation time, such as *C*. This can be done without necessitating rewriting of the code by using the *Cython* library. This allows for compilation of *Python* code into *C* code, yielding a significant boost in computation speed. Such an alteration was attempted but generated no significant improvement since the *mpmath* library, which handled the integration, was written in *Python*. For this reason, if the computations of this thesis are to be repeated, it might be preferential to consider an integration method more compatible with *Cython*, or change the implementation language altogether.

Furthermore, a grid was utilised to perform the integral over the lattice momentum $\boldsymbol{\ell}$ to further decrease overall computation time. This reduced the number of nested integrals without significant impact on the result. An additional response to the problem was parallelisation, which was used heavily. The calculation of $\frac{dR}{d\ln(E_{er})}$ is easily parallelisable for different $\mathbf{k}_\mathrm{f}$ and even different $\boldsymbol{\ell}$. Parallelisation over $\boldsymbol{\ell}$ was, however, not fully examined. In order to do this, another solution for the management of data shared between parallel executions would have to be developed.

Despite these efforts, the final calculations required extensive computational resources, as approximately 15,000 core hours were used throughout this project. As the final method still required significant computational power, any future recreations could be approached with additional approximations. Since the qualitative behaviour of the differential rates for different scattering amplitudes over E_{er} seems uncomplicated for the cases studied, one might suggest fixating E_{er}, thus only performing the calculation for the kinetic energy yielding the highest contribution. This would, however, not reveal the differences in rate decline with regard to the scattering amplitudes discussed in section 5.1.2. A further suggestion is to set the incoming DM velocity distribution $g(\mathbf{v})$ to a delta function, which would in all certainty aid the general case discussed in section 2.1.3, where the analytical evaluation of the $\mathbf{v}$ integral is not applicable. Making the grid over $\boldsymbol{\ell}$ more sparse is not a preferable approach due to the complicated dependence on $\boldsymbol{\ell}$ for the band energies and the constants C, as described in Figure B.1, although it might be possible for the π band. Finally, any results obtained from further numerical approximations of the calculations should be compared with the results of this thesis to determine if the current precision level is motivated.

5.3 Further research

As has been discussed, the constraints of time and computational resources restricted this thesis to cases where the scattering amplitude $\mathcal{M}$ is only dependent on the momentum transfer $\mathbf{q}$. This specifically entailed that no terms dependent on $\mathbf{v}_\mathrm{el}^\perp$ were

studied. In further research, this limitation ought to be rescinded, thus extending the amount of computable cases. This would enable the evaluation of interactions between DM particles and graphene valence electrons when DM is regraded as an anapole, magnetic dipole and electric dipole, in accordance with [25]. Such studies would require considerably more computational power as $\eta(v_{min})$ would not in general be analytically rewritable, possibly introducing a new momentum transfer dependent integral. Furthermore, the integral over the velocity $\mathbf{v}$ would not be analytically evaluable through the reformulation in Appendix A.2, since $\mathbf{v}_{\mathrm{el}}^{\perp}$ is dependent on $\mathbf{v}$. However, while these factors entail a significant computational burden, they by no means render the calculations impossible. With a strategic method and adequate computational power, these cases both can and should be studied.

Bibliography

[1] R. Gendler, *Andromeda Island Universe*, (2005) Available: https://apod.nasa.gov/apod/ap051222.html

[2] I. Newton *Philosophiae naturalis principia mathematica*. London, Royal Society, 1687.

[3] A. Einstein *Die Grundlage der allgemeinen Relativitätstheorie*. Annalen der Physik, vol. 354, no. 7, pp. 769–822, 1916. doi:10.1002/andp.1916354070 [Online]. Available: dx.doi.org/10.1002/andp.1916354070

[4] H. Poincare, *The Milky Way and the Theory of Gases*. Popular Astronomy, vol. 14, pp. 475–488, doi: CBO9781107252950.043 [Online]. Available: https://doi.org/10.1017/CBO9781107252950.043

[5] F. Zwicky, *Republication of: The redshift of extragalactic nebulae*. General Relativity and Gravitation , vol. 41, pp. 203–206, doi: 10.1007/s10714-008-0706-5 [Online]. Available: https://doi.org/10.1007/s10714-008-0706-5

[6] G. Bertone, D. Hooper, *History of dark matter*. Reviews of Modern Physics, vol. 90, no. 4, 2018. doi:10.1103/RevModPhys.90.045002 [Online]. Available: https://doi.org/10.1103/RevModPhys.90.045002

[7] H. W. Babcock, *The rotation of the Andromeda Nebula*. Lick Observatory Bulletin , vol. 19 no. 498, pp. 41-51, OCLC: 36394975 [Online]. Available: http://articles.adsabs.harvard.edu/pdf/1939LicOB..19...41B

[8] V. Rubin and K. Ford *Rotation of the Andromeda Nebula from a Spectroscopic Survey of Emission Regions*. Astrophysical Journal, vol. 159, pp. 379, doi: 10.1086/150317 [Online]. Available: https://doi.org/10.1086/150317

[9] K. Freeman *On the Disks of Spiral and S0 Galaxies*. Astrophysical Journal, vol. 160, pp. 811, doi: 10.1086/150474 [Online]. Available: https://doi.org/10.1086/150474

[10] J. M. Overduin and P. S. Wesson, *Dark matter and background light*. Physics Reports, vol. 402, no. 5–6, pp.267–406 , 2004. doi:10.1016/j.physrep.2004.07.006 [Online]. Available: dx.doi.org/10.1016/j.physrep.2004.07.006

[11] R. Massey, T. Kitching, and J. Richard, *The dark matter of gravitational lensing*. Reports on Progress in Physics, vol. 73, no. 8, 2010. doi:10.1088/0034-4885/73/8/086901 [Online]. Available: dx.doi.org/10.1088/0034-4885/73/8/086901

[12] G. Sharma, Anu and B. C. Chauhan, *Dark Matter and Neutrinos*. arXiv preprint arXiv:1711.10564. [Online]. Available: https://arxiv.org/pdf/1711.10564.pdf

[13] C. Quigg, *Cosmic neutrinos*. arXiv preprint arXiv:0802.0013. [Online]. Available: https://arxiv.org/pdf/0802.0013.pdf

[14] K. Griest, *The Search for the Dark Matter: WIMPs and MACHOs*. arXiv preprint arXiv:hep-ph/9303253. [Online]. Available: https://arxiv.org/pdf/hep-ph/9303253.pdf

[15] M. S. Roberts, R. N. Whitehurst, *The rotation curve and geometry of M31 at large galactocentric distances*. Astrophysical Journal, vol. 201, pp. 327–346 , 1975. doi:10.1086/153889 [Online]. Available: https://doi.org/10.1086/153889

[16] M. Fukugita and P. Peebles, *The Cosmic Energy Inventory*. The Astrophysical Journal, vol. 616, no. 2 , 2004. doi:10.1086/425155 [Online]. Available: https://doi.org/10.1086/425155

[17] E. Aprile, *The XENON Dark Matter Search*. Journal of Physics: Conference Series, vol. 308, doi: :10.1088/1742-6596/308/1/012010 [Online]. Available: https://iopscience.iop.org/article/10.1088/1742-6596/308/1/012010/pdf

[18] J. Conrad, *Indirect Detection of WIMP Dark Matter: a compact review*. arXiv preprint arXiv:1411:1925. [Online]. Available: https://arxiv.org/pdf/1411:1925.pdf

[19] T. Marrodán Undagoitia and L. Rauch, *Dark matter direct-detection experiments*. Journal of Physics G: Nuclear and Particle Physics, vol. 43, no. 1, doi: 10.1088/0954-3899/43/1/013001 [Online]. Available: https://doi.org/10.1088/0954-3899/43/1/013001

[20] Y. Hochberg, Y. Kahn, M. Lisanti, C. G. Tully and K. M. Zurek, *Directional detection of dark matter with two-dimensional targets*. Physics Letters B, vol. 772, no. 239–246, pp. 239–246 , 2017. doi:10.1016/j.physletb.2017.06.051 [Online]. Available: http://dx.doi.org/10.1016/j.physletb.2017.06.051

[21] E. Baracchini, M.G. Betti, M. Biasotti, A. Bosca, F. Calle, J. Carabe-Lopez, G. Cavoto, C. Chang, A.G. Cocco, A.P. Colijn, et al., *PTOLEMY: A proposal for thermal relic detection of massive neutrinos and directional detection of MeV dark matter*. arXiv preprint arXiv:1808.01892. [Online]. Available: https://arxiv.org/abs/1808.01892

[22] F. Mandl and G: Shaw, *Quantum field theory*. Manchester, John Wiley & Sons, 2010.

[23] R. Catena and P. Ullio, *A novel determination of the local dark matter density*. Journal of Cosmology and Astroparticle Physics, vol. 08, no. 004, 2010, doi: 10.1088/1475-7516/2010/08/004 [Online]. Available: https://doi.org/10.1088/1475-7516/2010/08/004

[24] R. Catena, T. Emken, N. Spaldin and W. Tarantino, *Atomic responses to general dark matter-electron interactions*. arXiv preprint arXiv:1912.08204. [Online]. Available: https://arxiv.org/pdf/1912.08204.pdf

[25] R. Catena, T. Emken and J. Ravanis, *Rejecting the Majorana nature of dark matter with electron scattering experiments*. arXiv preprint arXiv:2003.04039. [Online]. Available: https://arxiv.org/pdf/2003.04039.pdf

[26] G. Dresselhaus, S. Riichiro and M.S. Dresselhaus, *Physical properties of carbon nanotubes*. London, Imperial College Press, 1998.

[27] J. Andersson, E. Grönfors, C. Hellekant, L. Lindblad and F. Resare, *DM-rate-calculation-in-graphene* Available: https://github.com/LudvigLindblad/DM-rate-calculation-in-graphene

[28] R. Essig, M. Fernandez-Serra, J. Mardon, A. Soto, T. Volansky and T. Yua, *Direct Detection of sub-GeV Dark Matter with Semiconductor Targets*. arXiv preprint arXiv:1509.01598. [Online]. Available: https://arxiv.org/pdf/1509.01598.pdf

A

Physical Properties of Dark Matter

In the following appendix the distribution and limitations of the DM velocity is presented. Furthermore, a more computable reformulation of the DM induced electron ejection rate is derived. Lastly, limits of the momentum transfer are presented as well.

A.1 Velocity Distribution of Dark Matter

The physical properties of DM have been assumed to be in accordance with the SHM hypothesis. This entails that the velocity distribution of DM follows a Maxwell-Boltzmann distribution boosted from the galactic rest frame into the laboratory frame. The velocity can, however, not be infinite. The distribution is thus truncated at a maximal velocity given by the galactic escape velocity, $v_{\max} = v_{\text{esc}} + v_{\oplus}$, i.e. the minimal velocity necessary to escape the gravitational influence of the Milky Way. The velocity distribution, $g(\mathbf{v})$, is then given as

$$g(\mathbf{v}) = \frac{1}{N_{\text{esc}}\pi^{3/2}v_0^3}\exp\left[-\frac{(\mathbf{v}+\mathbf{v}_{\oplus})^2}{v_0^2}\right] \times \Theta\left(v_{\text{esc}} - |\mathbf{v}+\mathbf{v}_{\oplus}|\right), \tag{A.1}$$

where $N_{\text{esc}} \equiv \text{erf}(v_{\text{esc}}/v_0) - 2(v_{\text{esc}}/v_0)\exp(-v_{\text{esc}}^2/v_0^2)/\sqrt{\pi}$ is a normalisation constant. Furthermore $v_0 = 220$ km/s is the orbital velocity of the sun and $v_{\text{esc}} = 544$ km/s is the galactic escape velocity. The velocity of the Earth, and thus the observer, in the galactic rest frame is $v_{\oplus} \approx 244$ km/s [24].

As has been explained, the DM velocity distribution in the local halo has a maximal velocity, placing an upper boundary $v_{\max} = v_{\text{esc}} + v_{\oplus}$ on the integration limit. The ionisation of bound electrons also necessitate a lower limit of the velocity such that $v_{\min} < v_{\max} = v_{\text{esc}} + v_{\oplus}$. This minimal velocity is given as

$$v_{\min}(k_{\text{f}}, q, \boldsymbol{\ell}) = \frac{{k_{\text{f}}}^2/(2m_e) + E_i(\boldsymbol{\ell}) + \Phi}{q} + \frac{q}{2m_\chi} \tag{A.2}$$

and is derived in Appendix A.2. Thus, $v \in (v_{\min}, v_{\max})$ constitute an integration interval in section 3.2.

A.2 Reformulation of the Ejection Rate

From the steps shown in Section 2.1.2 we have derived the DM induced electron ejection rate as

$$R = 2 \sum_{i=\pi,\sigma_1,\sigma_2,\sigma_3} \frac{\rho_\chi}{m_\chi} N_c A_{uc} \int \frac{d^2\ell}{(2\pi)^2} \int d^3v g(\mathbf{v}) v \sigma_i(\boldsymbol{\ell}), \tag{A.3}$$

i.e. equation (2.38). We denote the contribution from each band with R_i, $i = \pi, \sigma_1, \sigma_2, \sigma_3$, and thus we have

$$\begin{aligned} R_i = \frac{\bar{\sigma_e}}{\mu_{e\chi}^2} \int \frac{d^3k_\mathrm{f}}{(2\pi)^3} \int \frac{d^3q}{4\pi} \left|F_{DM}(\mathbf{q}, \mathbf{v}_\mathrm{el}^\perp)\right|^2 \left|\tilde{\psi}_i(\boldsymbol{\ell}, \mathbf{q} - \mathbf{k}_\mathrm{f})\right|^2 \\ \times \delta\left(E_{er} + E_i(\boldsymbol{\ell}) + \Phi + \frac{q^2}{2m_\chi} - qv\cos\theta_{qv}\right). \end{aligned} \tag{A.4}$$

Here we have specified the difference between final and initial energies $E_f - E_i$. Note that $E_{er} = k_\mathrm{f}^2/2m_e$. Let us now consider the integral over the incoming velocity v. This tridimensional integral can be rewritten in spherical coordinates. A preferential approach is to project the coordinate system onto the direction of $\mathbf{q}$. We then get

$$\int d^3v = \int dv v^2 \int_0^{2\pi} d\phi \int_{-1}^{1} d\cos\theta_{qv}. \tag{A.5}$$

Before we implement this change of variables into equation (A.4), let us study the delta function. It can be rewritten as

$$\frac{1}{qv}\delta\left(\cos\theta_{qv} - \frac{E_{er} + E_i(\boldsymbol{\ell}) + \Phi}{qv} + \frac{q}{2m_\chi v}\right). \tag{A.6}$$

The delta function now demands that

$$\cos\theta_{qv} = \frac{E_{er} + E_i(\boldsymbol{\ell}) + \Phi}{qv} + \frac{q}{2m_\chi v} < 1, \tag{A.7}$$

where the inequality follows from the definition of cosine. From this we can calculate a lower bound on v as

$$v_\mathrm{min} = \frac{E_{er} + E_i(\boldsymbol{\ell}) + \Phi}{q} + \frac{q}{2m_\chi}, \tag{A.8}$$

which is the origin of the expression given in equation (A.2). The change of variables can now be implemented into equation (A.5), which gives

$$\begin{aligned} R = 2 \sum_{i=\pi,\sigma_1,\sigma_2,\sigma_3} \frac{\rho_\chi}{m_\chi} N_c A_{uc} \frac{\bar{\sigma_e}}{\mu_{e\chi}^2} \int \frac{d^2\ell}{(2\pi)^2} \int \frac{d^3k_\mathrm{f}}{(2\pi)^3} \int \frac{d^3q}{4\pi} \frac{2\pi}{q} \int_{v>v_\mathrm{min}} dv \frac{v^2}{v} g(v) \times \\ \left|F_{DM}(\mathbf{q}, \mathbf{v}_\mathrm{el}^\perp)\right|^2 \left|\tilde{\psi}_i(\boldsymbol{\ell}, \mathbf{q} - \mathbf{k}_\mathrm{f})\right|^2. \end{aligned} \tag{A.9}$$

Let us now, for the sake of simplification, define a function

$$\eta = \int\limits_{v>v_{\min}} d\Omega_{qv} \int dv \cdot v g(v), \tag{A.10}$$

and then get

$$\begin{aligned} R = 2 \sum_{i=\pi,\sigma_1,\sigma_2,\sigma_3} \frac{\rho_\chi}{m_\chi} N_c A_{uc} \frac{\bar{\sigma_e}}{\mu_{e\chi}^2} \int \frac{d^2\ell}{(2\pi)^2} \int \frac{d^3k_\mathrm{f}}{(2\pi)^3} \int \frac{d^3q}{4\pi} \frac{\pi}{q} \eta(v_{\min}) \\ \times \left| F_{DM}(\mathbf{q}, \mathbf{v}_\mathrm{el}^\perp) \right|^2 \left| \tilde{\psi}_i(\boldsymbol{\ell}, \mathbf{q} - \mathbf{k}_\mathrm{f}) \right|^2 . \end{aligned} \tag{A.11}$$

We recall that $E_{er} = k_\mathrm{f}^2/2m_e$ and can now study the integral over k_f. This is another tridimensional integral which can also be rewritten in spherical coordinates as

$$\int d^3k_\mathrm{f} = \int k_\mathrm{f}^2 dk_\mathrm{f} \int d\Omega_{k_\mathrm{f}}, \tag{A.12}$$

where Ω_{k_f} is the solid angle. From the definition of E_{er} we get

$$k_\mathrm{f}^2 dk_\mathrm{f} = m_e k_\mathrm{f} dE_{er} \longrightarrow dE_{er} = \frac{2k_\mathrm{f} dk_\mathrm{f}}{2m_e}. \tag{A.13}$$

We also know that

$$dE_{er} = E_{er} d\ln(E_{er}), \tag{A.14}$$

and thus

$$dk_\mathrm{f} = \frac{k_\mathrm{f}}{2} d\ln(E_{er}). \tag{A.15}$$

In combination with equation (A.12), we thus have

$$\int \frac{d^3k_\mathrm{f}}{(2\pi)^3} = \frac{1}{(2\pi)^3} \frac{k_\mathrm{f}^3}{2} \int d\ln(E_{er}) \int d\Omega_{k_\mathrm{f}}. \tag{A.16}$$

If we implement this last change of variables we finally get

$$\begin{aligned} \frac{dR}{d\ln(E_{er})} = 2 \sum_{i=\pi,\sigma_1,\sigma_2,\sigma_3} \frac{\rho_\chi}{m_\chi} N_c A_{uc} \frac{\bar{\sigma_e}}{\mu_{e\chi}^2} \int \frac{d^2\ell}{(2\pi)^2} \int \frac{d\Omega_{k_\mathrm{f}}}{(2\pi)^3} \frac{k_\mathrm{f}^3}{2} \int\limits_{v_{\max}}^{v_{\max}} \frac{d^3q}{4\pi} \frac{\pi}{q} \eta(v_{\min}) \\ \times \left| F_{DM}(\mathbf{q}, \mathbf{v}_\mathrm{el}^\perp) \right|^2 \left| \tilde{\psi}_i(\boldsymbol{\ell}, \mathbf{q} - \mathbf{k}_\mathrm{f}) \right|^2 . \end{aligned} \tag{A.17}$$

A.3 Analytical Evaluation of η

By regarding the velocity distribution, described in Appendix A.1, with a single, overall normalisation constant N_η, we get

$$g(\mathbf{v}) = \frac{1}{N_\eta} \exp\left[-\frac{(\mathbf{v} + \mathbf{v}_\oplus)^2}{v_0^2} \right] \times \Theta\left(v_\mathrm{esc} - |\mathbf{v} + \mathbf{v}_\oplus| \right). \tag{A.18}$$

In accordance with equation (A.1) and [28], N_η is then given as

$$N_\eta = v_0^3 \pi \left[\mathrm{erf}(\frac{v_{esc}}{v_0}) - 2\frac{v_{esc}}{v_0} e^{-(\frac{v_{esc}}{v_0})^2} \right]. \tag{A.19}$$

From equation (A.1), and consequently (A.18), the minimal velocity v_{min} is given as

$$v_{\mathrm{min}} = \frac{E_{er} + E_i(\boldsymbol{\ell}) + \Phi}{q} + \frac{q}{2m_\chi}. \tag{A.20}$$

Furthermore, $\eta(v_{\mathrm{min}})$ is defined as

$$\eta(v_{\mathrm{min}}) = \int \frac{d^3v}{v} g(v) \Theta(v - v_{\mathrm{min}}). \tag{A.21}$$

We also get

$$\eta(v_{\mathrm{min}}) = \frac{1}{N_\eta} \int 2\pi d\cos\theta dv_\chi v_\chi \exp\left(-\frac{v_\chi^2 + v_{\mathrm{esc}} - 2vv_\oplus \cos\theta}{v_0^2} \right) \Theta(v_\chi - v_{\mathrm{min}}) \Theta(v_{\mathrm{esc}} - v_\chi). \tag{A.22}$$

In order to solve the equality between equations (A.21) and (A.22) we need to consider the following two cases:

$$\begin{cases} 1. & v_{\mathrm{min}} < v_{\mathrm{esc}} - v_\oplus \\ 2. & v_{\mathrm{esc}} - v_\oplus < v_{\mathrm{min}} < v_{\mathrm{esc}} + v_\oplus. \end{cases} \tag{A.23}$$

Through some algebraic manipulation, this gives us the solutions $\eta_1(v_{\mathrm{min}})$ and $\eta_2(v_{\mathrm{min}})$ as

$$\begin{aligned} \eta_1(v_{min}) &= \frac{v_0^2 \pi}{2v_\oplus N_\eta} \Big(-4e^{-v_{esc}^2/{v_0}^2} v_\oplus + \sqrt{\pi} v_0 \Big[\mathrm{erf}\left(\frac{v_{min} + v_\oplus}{v_0} \right) - \mathrm{erf}\left(\frac{v_{min} - v_E}{v_0} \right) \Big] \Big) \\ \eta_2(v_{min}) &= \frac{v_0^2 \pi}{2v_\oplus N_\eta} \Big(-2e^{-v_{esc}^2/{v_0}^2} (v_{esc} - v_{min} + v_\oplus) + \sqrt{\pi} v_0 \Big[\mathrm{erf}\left(\frac{v_{esc}}{v_0} \right) - \\ &\qquad \mathrm{erf}\left(\frac{v_{min} - v_\oplus}{v_0} \right) \Big] \Big). \end{aligned} \tag{A.24}$$

These solutions are equal when $v_{\mathrm{min}} = v_{\mathrm{esc}} - v_\oplus$.

A.4 Limits of the Momentum Transfer Integral

The delta function places a restriction on the values of the momentum transfer $\mathbf{q}$. Since the minimal energy needed for ionisation must exceed $E_{er} + E_i(\boldsymbol{\ell}) + \Phi$, we can now, from equation (A.20), derive a range of allowed momentum transfer. This is done by inferring $\cos\theta_{qv} = 1$ and recalling that the minimum DM velocity v_{min} in the laboratory reference frame must fulfill $v_{\mathrm{min}} < v_{\mathrm{max}} = v_{\mathrm{esc}} + v_\oplus$. The resulting integration limits placed on $\mathbf{q}$ are then given as

$$\begin{aligned} q_{\mathrm{max}} &= m_\chi v_{\mathrm{max}} + \sqrt{m_\chi^2 v_{\mathrm{max}}^2 - \frac{m_\chi}{m_e} k_{\mathrm{f}}^2 - 2m_\chi \left(E_i(\boldsymbol{\ell}) + \Phi \right)} \\ q_{\mathrm{min}} &= m_\chi v_{\mathrm{max}} - \sqrt{m_\chi^2 v_{\mathrm{max}}^2 - \frac{m_\chi}{m_e} k_{\mathrm{f}}^2 - 2m_\chi \left(E_i(\boldsymbol{\ell}) + \Phi \right)}. \end{aligned} \tag{A.25}$$

B

Physical Properties of Graphene

The following appendix describes the definition, Fourier transform and normalisation of the wave functions of graphene valence electrons. Furthermore, the lattice structure and first Brilluoin zone of graphene are presented.

B.1 Wave Functions of Graphene

Graphene has four valence electrons, occupying $2s2p^3$ orbitals. Unhybridised p_z orbitals create covalent π bonds while $2s$ hybridisation with p_x and p_y orbitals form σ bonds. In general, a tight binding Bloch function is given by

$$\Phi_j(\boldsymbol{\ell}, \mathbf{r}) = \frac{1}{\sqrt{N}} \sum_N e^{i\boldsymbol{\ell}\cdot\mathbf{R}_N} \varphi_j(\mathbf{r} - \mathbf{R}_N), \tag{B.1}$$

where $j = 1, \cdots, n$ and φ_j is the atomic orbital. In accordance with the tight binding model, the sum only runs over the closest atoms, which in graphene are three other carbon atoms. The position vectors of the nearest atoms, $\mathbf{R_1}$, $\mathbf{R_2}$ and $\mathbf{R_3}$, are defined in Figure B.3 of appendix B.2. For every atomic orbital ϕ, it follows that

$$\begin{aligned} \Phi_A(\boldsymbol{\ell}, \mathbf{r}) &= \phi(\mathbf{r}), \\ \Phi_B(\boldsymbol{\ell}, \mathbf{r}) &= \frac{f(\boldsymbol{\ell})}{\sqrt{3}} \phi\left(\mathbf{r} - \mathbf{R}_j\right), \end{aligned} \tag{B.2}$$

where $f(\boldsymbol{\ell}) = \sum_{j=1}^{3} e^{i\boldsymbol{\ell}\cdot\mathbf{R}_j}$. The eigenfunctions are expressed by a linear combination of the Bloch functions according to

$$\Psi_i(\boldsymbol{\ell}, \mathbf{r}) = \sum_{j=1}^{n} C_{ij}(\boldsymbol{\ell}) \Phi_j(\boldsymbol{\ell}, \mathbf{r}). \tag{B.3}$$

The stationary Schrödinger equation,

$$H\Psi_i = E_i(\boldsymbol{\ell})\Psi_i, \tag{B.4}$$

is satisfied for all eigenfunctions. Here, H is the crystal Hamiltonian and $E_i(\boldsymbol{\ell})$ is the band energy. By denoting $\mathcal{S}$ as the overlapping integral matrix and $\mathcal{H}$ as the transfer integral matrix, equation (B.4) can be expressed as

$$\mathcal{H}\mathbf{C}_i = E_i(\boldsymbol{\ell})\mathcal{S}\mathbf{C}_i, \tag{B.5}$$

from which the band energies E_i and corresponding eigenvectors $\mathbf{C}_i$ can be calculated.

B.1.1 The π band Wave Function

The unhybridised π orbital is given by the wave function

$$\psi_\pi(\boldsymbol{\ell}, \mathbf{r}) \approx N_\pi(\boldsymbol{\ell}) \left(\phi_{2\mathrm{p_z}}(\mathbf{r}) C_1 + C_2 f(\boldsymbol{\ell}) \phi_{2\mathrm{p_z}}(\mathbf{r} - \mathbf{R}_j)\right), \tag{B.6}$$

where the wave function for the $2p_z$ orbital is hydrogenic and thus given by

$$\phi_{2\mathrm{p_z}}(\mathbf{r}) = N_{2p_z} a_0^{-3/2} \frac{r}{a_0} e^{Z_{\mathrm{eff}}^{2\mathrm{p_z}} r/2a_0} \cos\theta. \tag{B.7}$$

Here, $a_0 = 0.529\,\text{Å}$ is the Bohr radius and $Z_{\mathrm{eff}}^{2\mathrm{p_z}} = 4.03$ is the $2p_z$ specific effective potential. Furthermore, the Fourier transform of ψ_π is given as

$$\mathcal{F}(\psi_\pi)(\boldsymbol{\ell}, \mathbf{k}) = \widetilde{N}_\pi(\boldsymbol{\ell}) \left(C_1 + C_2 f(\boldsymbol{\ell} + \mathbf{k})\right) \mathcal{F}(\phi_{2\mathrm{p_z}})(\mathbf{k}), \tag{B.8}$$

where the Fourier transform of the $2p_z$ orbital can be approximated by

$$\mathcal{F}(\phi_{2\mathrm{p_z}})(\mathbf{k}) \approx \widetilde{N}_{2p_z} a_0^{3/2} \frac{a_0 k_z}{\left(a_0^2 |\mathbf{k}|^2 + \left(Z_{\mathrm{eff}}^{2\mathrm{p_z}}/2\right)^2\right)^3}. \tag{B.9}$$

The coefficients as well as the π band energy can be calculated from equation (B.5). The overlapping integral matrix and the transfer integral matrix for π are

$$\mathcal{S} = \begin{pmatrix} 1 & s f(\boldsymbol{\ell}) \\ s f(\boldsymbol{\ell})^* & 1 \end{pmatrix}, \quad \mathcal{H} = \begin{pmatrix} \epsilon_{2p} & t f(\boldsymbol{\ell}) \\ t f(\boldsymbol{\ell})^* & \epsilon_{2p} \end{pmatrix}, \tag{B.10}$$

where $s = 0.129$ is the overlap integral and $t = -3.03\,\text{eV}$ is the transfer integral between nearest neighbours. Moreover, $\epsilon_{2s} = -8.87$ eV is given relative to ϵ_{2p} and hence $\epsilon_{2p} = 0$ is chosen for the sake of simplicity [20].

Solving for the eigenenergy in equation (B.5) results in

$$E_\pi(\boldsymbol{\ell}) = \frac{\epsilon_{2p} \pm t|f(\boldsymbol{\ell})|}{1 \pm s|f(\boldsymbol{\ell})|}, \tag{B.11}$$

where $\pm$ correspond to valence and conductivity bands, respectively. The corresponding eigenvector to these eigenenergies is given as

$$\mathbf{C}(\boldsymbol{\ell}) = \begin{pmatrix} C_1(\boldsymbol{\ell}) \\ C_2(\boldsymbol{\ell}) \end{pmatrix} = \frac{1}{\sqrt{2}} \begin{pmatrix} 1 \\ \pm \frac{e^{i\varphi_{\boldsymbol{\ell}}}}{\sqrt{3}} \end{pmatrix} \tag{B.12}$$

B.1.2 The σ band Wave Functions

The σ wave functions are linear combinations of $2s$, $2p_x$ and $2p_y$ orbitals as a result of the sp^2 hybridisation in graphene. These orbitals are hydrogenic and thus given by

$$
\begin{aligned}
\phi_{2\mathrm{p}_x}(\mathbf{r}) &= N_{2p_x,2p_y} a_0^{-3/2} \frac{r}{a_0} e^{-Z_{\mathrm{eff}}^{2\mathrm{p}_x/2\mathrm{p}_y} r/2a_0} \sin\theta\cos\varphi, \\
\phi_{2\mathrm{p}_y}(\mathbf{r}) &= N_{2p_x,2p_y} a_0^{-3/2} \frac{r}{a_0} e^{-Z_{\mathrm{eff}}^{2\mathrm{p}_x/2\mathrm{p}_y} r/2a_0} \sin\theta\sin\varphi, \\
\phi_{2\mathrm{s}}(\mathbf{r}) &= N_{2s} a_0^{-3/2} \left(1 - \frac{Z_{\mathrm{eff}}^{2\mathrm{s}} r}{a_0}\right) e^{-Z_{\mathrm{eff}}^{2\mathrm{s}} r/2a_0}.
\end{aligned}
\tag{B.13}
$$

The Fourier transform of the $2s$ orbital can be calculated analytically, while the Fourier transforms of the $2p_x$ and $2p_y$ orbitals can only be approximated. These Fourier transforms result in

$$
\begin{aligned}
\tilde{\phi}_{2\mathrm{p}_x}(\mathbf{k}) &\approx \widetilde{N}_{2p_x,2p_y} a_0^{3/2} \frac{a_0 k_x}{\left(a_0^2|\mathbf{k}|^2 + \left(Z_{\mathrm{eff}}^{2\mathrm{p}_x/2\mathrm{p}_y}/2\right)^2\right)^3}, \\
\tilde{\phi}_{2\mathrm{p}_y}(\mathbf{k}) &\approx \widetilde{N}_{2p_x,2p_y} a_0^{3/2} \frac{a_0 k_y}{\left(a_0^2|\mathbf{k}|^2 + \left(Z_{\mathrm{eff}}^{2\mathrm{p}_x/2\mathrm{p}_y}/2\right)^2\right)^3}, \\
\tilde{\phi}_{2\mathrm{s}}(\mathbf{k}) &= \widetilde{N}_{2s} a_0^{3/2} \frac{a_0^2|\mathbf{k}|^2 - \left(Z_{\mathrm{eff}}^{2\mathrm{s}}/2\right)^2}{\left(a_0^2|\mathbf{k}|^2 + \left(Z_{\mathrm{eff}}^{2\mathrm{s}}/2\right)^2\right)^3},
\end{aligned}
\tag{B.14}
$$

with orbital specific effective potentials, $Z_{\mathrm{eff}}^{2\mathrm{p}_x/2\mathrm{p}_y} = 5.49$ and $Z_{\mathrm{eff}}^{2\mathrm{s}} = 4.84$, as given by Hochberg et al. [20].

As presented in [26], and further detailed by Hochberg et al. [20], the band energies are obtained from equation (B.5). For σ, the $\mathcal{S}$ and $\mathcal{H}$ matrices are obtained by assembling the sub matrices $\mathcal{S}_{AA}$, $\mathcal{S}_{AB}$, $\mathcal{S}_{BA}$, $\mathcal{S}_{BB}$ and $\mathcal{H}_{AA}$, $\mathcal{H}_{AB}$,$\mathcal{H}_{BA}$, $\mathcal{H}_{BB}$. The sub matrices for $\mathcal{S}$ are given as

$$
\mathcal{S}_{AA} = \begin{pmatrix} 1 & 0 & 0 \\ 0 & 1 & 0 \\ 0 & 0 & 1 \end{pmatrix} \quad \mathcal{S}_{AB} = \begin{pmatrix} \mathcal{S}_{\mathrm{ss}} & \mathcal{S}_{\mathrm{sp}_x} & \mathcal{S}_{\mathrm{sp}_y} \\ -\mathcal{S}_{\mathrm{sp}_x} & \mathcal{S}_{\mathrm{p_x p_x}} & \mathcal{S}_{\mathrm{p_x p_y}} \\ -\mathcal{S}_{\mathrm{sp}_y} & \mathcal{S}_{\mathrm{p_x p_y}} & \mathcal{S}_{\mathrm{p_y p_y}} \end{pmatrix},
\tag{B.15}
$$

with matrix elements as

$$
\begin{aligned}
\mathcal{S}_{\mathrm{ss}} &= S_{\mathrm{ss}} \left(e^{i\ell_x a} + 2e^{-i\ell_x a/2} \cos\left(\frac{\sqrt{3}\ell_y a}{2}\right)\right) \\
\mathcal{S}_{\mathrm{sp}_x} &= S_{\mathrm{sp}} \left(-e^{i\ell_x a} + e^{-i\ell_x a/2} \cos\left(\frac{\sqrt{3}\ell_y a}{2}\right)\right) \\
\mathcal{S}_{\mathrm{sp}_y} &= -i\sqrt{3} S_{\mathrm{sp}} e^{-i\ell_x a/2} \sin\left(\frac{\sqrt{3}\ell_y a}{2}\right) \\
\mathcal{S}_{\mathrm{p}_x\mathrm{p}_x} &= -S_\sigma e^{i\ell_x a} + \frac{(3S_\pi - S_\sigma)}{2} e^{-i\ell_x a/2} \cos\left(\frac{\sqrt{3}\ell_y a}{2}\right) \\
\mathcal{S}_{\mathrm{p}_x\mathrm{p}_y} &= \frac{i\sqrt{3}}{2} \left(S_\sigma + S_\pi\right) e^{-i\ell_x a/2} \sin\left(\frac{\sqrt{3}\ell_y a}{2}\right) \\
\mathcal{S}_{\mathrm{p}_y\mathrm{p}_y} &= S_\pi e^{i\ell_x a} + \frac{(S_\pi - 3S_\sigma)}{2} e^{-i\ell_x a/2} \cos\left(\frac{\sqrt{3}\ell_y a}{2}\right).
\end{aligned}
\tag{B.16}
$$

The sub matrices of $\mathcal{H}$ are given as

$$\mathcal{H}_{AA} = \begin{pmatrix} \epsilon_{2\mathrm{s}} & 0 & 0 \\ 0 & \epsilon_{2\mathrm{p}} & 0 \\ 0 & 0 & \epsilon_{2\mathrm{p}} \end{pmatrix}, \mathcal{H}_{AB} = \begin{pmatrix} \mathcal{H}_{\mathrm{ss}} & \mathcal{H}_{\mathrm{sp}_x} & \mathcal{H}_{\mathrm{sp}_y} \\ -\mathcal{H}_{\mathrm{sp}_x} & \mathcal{H}_{\mathrm{p}_x\mathrm{p}_x} & \mathcal{H}_{\mathrm{p}_x\mathrm{p}_y} \\ -\mathcal{H}_{\mathrm{sp}_y} & \mathcal{H}_{\mathrm{p}_x\mathrm{p}_y} & \mathcal{H}_{\mathrm{p}_y\mathrm{p}_y} \end{pmatrix}, \tag{B.17}$$

with elements given in accordance with [26]. The AA transfer matrices are identical to the BB matrices. AB and BA are the overlap matrices, where BA is the hermitian transpose of AB for both $\mathcal{S}$ and $\mathcal{H}$. $\mathcal{H}_{AB}$ is obtained by replacing $\mathcal{S}$ with $\mathcal{H}$ and the S constants with H constants in equation (B.16). Both the overlap constants S and the transfer constants H, can be found in table B.1. For further details see Hochberg et al [20] and [26]. These analytical expressions can now be used to describe the eigenenergies associated with the wave functions of σ, and thus the Fourier transformed wave functions used in equation (2.37). The final wave functions $\widetilde{\psi}_{\sigma_i}$ are composed of a superposition of the valence orbitals $2p_x$, $2p_y$ and $2s$ as shown in equation (B.18).

$$\psi_{\sigma_i} = \mathbf{C}_i \begin{bmatrix} \phi_{2s}(\mathbf{r}) \\ \phi_{2p_x}(\mathbf{r}) \\ \phi_{2p_y}(\mathbf{r}) \\ \frac{1}{\sqrt{3}} \sum_j \phi_{2s}(\mathbf{r} - \mathbf{R}_j) e^{i\boldsymbol{\ell}\cdot\mathbf{R}_j} \\ \frac{1}{\sqrt{3}} \sum_j \phi_{2p_x}(\mathbf{r} - \mathbf{R}_j) e^{i\boldsymbol{\ell}\cdot\mathbf{R}_j} \\ \frac{1}{\sqrt{3}} \sum_j \phi_{2p_y}(\mathbf{r} - \mathbf{R}_j) e^{i\boldsymbol{\ell}\cdot\mathbf{R}_j} \end{bmatrix} \tag{B.18}$$

$\mathbf{C}_i = [C_1, C_2, C_3, C_4, C_5, C_6]_i$ represents the eigenvector associated with the each valence band. These can be calculated from the secular equation (B.5) for any given $\boldsymbol{\ell}$. The coefficients describing the superposition as well as the eigenenergies were tabulated on a 500×500 grid over the first Brillouin zone to aid the numerical calculation.

The overlap and transfer parameters used in the calculations where provided by Hochberg et al. [20] and are shown in Table (B.1).

Table B.1: Overlap and transfer parameters used in the calculations of σ band energies and wave functions.

$\mathcal{S}$	value	$\mathcal{H}$	value (eV)
S_{sp}	0.16	H_{sp}	-5.58
S_{ss}	0.21	H_{ss}	-6.77
S_{σ}	0.15	H_{σ}	-5.04
S_{π}	0.13	H_{π}	-3.03

The eigenvector components of the σ bands are plotted for reference in Figure B.1 over the first Brillouin zone. Since σ_1 and σ_2 are $2s$ dominated, a larger contribution from $C_{1,4}$ is expected. The σ_3 band, on the other hand, is largely affected by the $C_{2,5}$ and $C_{3,6}$ maps.

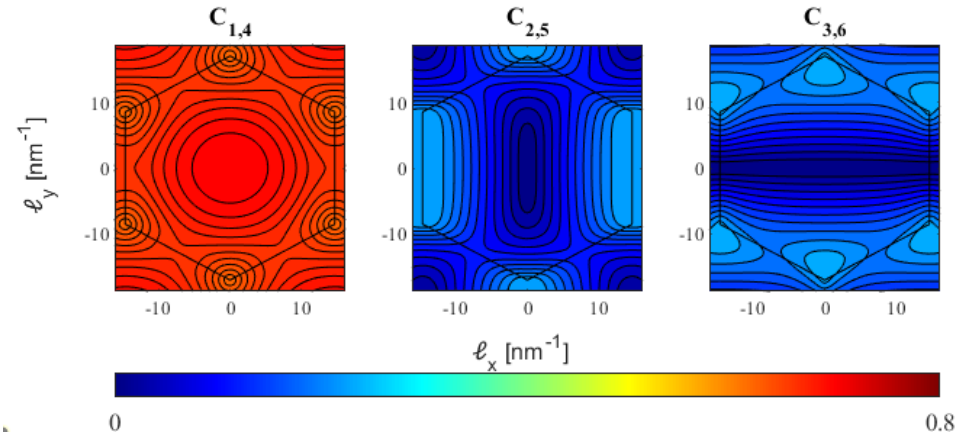

(a) σ_1

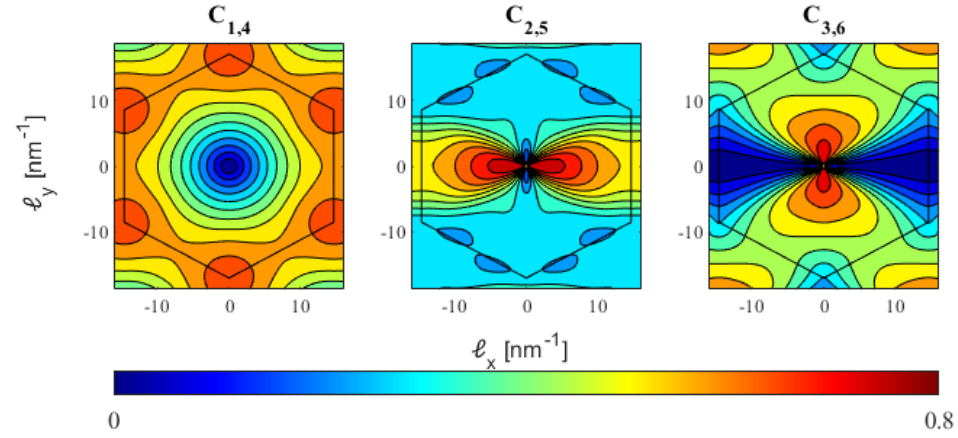

(b) σ_2

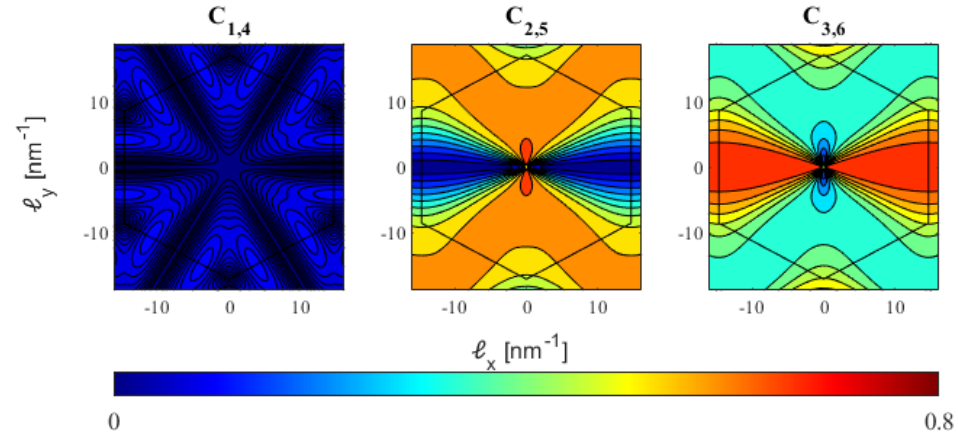

(c) σ_3

Figure B.1: Weighted contribution from $2s$, $2p_x$ and $2p_y$ for each respective σ shown by scalar factor and with the first Brillouin zone for reference. Note that σ_1 is mostly dominated by $2s$, as is σ_2, while σ_3 is mostly comprised by a combination of $2p_x$ and $2p_y$. Every graph represents two eigenvector elements: one for the contribution from Φ_A and one for Φ_B.

The binding energy of each valence band over the first Brillouin zone can be plotted in relation to the high symmetry points K, Γ and M, shown in Figure B.2. The σ_2 and σ_3 bands are mostly contributed to from near the edge of the first Brillouin zone, manifesting in a larger contribution to the differential rate from this area.

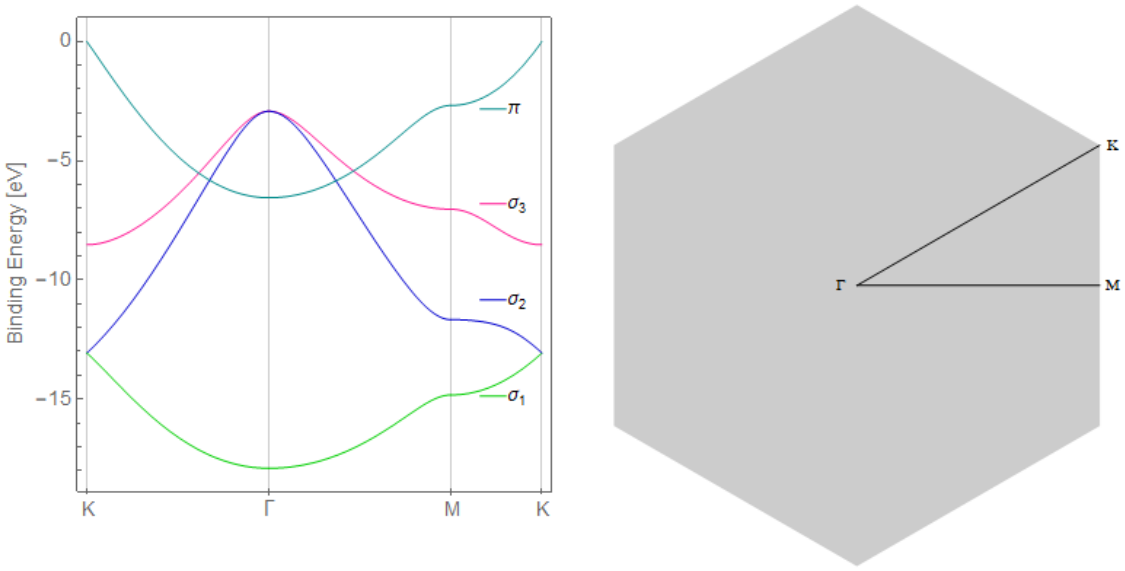

Figure B.2: Electronic band structure in the valence bands of graphene plotted against $\boldsymbol{\ell}$ with high-symmetry points K, Γ and M labelled. These symmetry points are visualised in the figure to the right.

B.1.3 Normalisation of the Wave Functions

The normalisation constants for the atomic orbital wave functions, $2s$, $2p_x$, $2p_y$ and $2p_z$ are given as

$$N_{2p_x,2p_y} = \frac{\sqrt{{Z_{\text{eff}}^{2\text{p}_\text{x}/2\text{p}_\text{y}}}^7}}{\pi}, \quad N_{2p_z} = \frac{\sqrt{{Z_{\text{eff}}^{2\text{p}_\text{z}}}^7}}{\pi}, \quad N_{2s} = \frac{\sqrt{{Z_{\text{eff}}^{2\text{s}}}^5}}{\pi}. \tag{B.19}$$

The Fourier transformed wave function for the π band must also be unit normalised. The normalisation constant in equation (B.8) is possible to calculate analytically. This is done according to

$$\begin{aligned}(2\pi)^3 = \left\langle \tilde{\Psi}_\pi \middle| \tilde{\Psi}_\pi \right\rangle = \widetilde{N}_\pi(\boldsymbol{\ell})^2 \left\langle C_1\Phi_A + C_2\Phi_B | C_1\Phi_A + C_2\Phi_B \right\rangle = \\ = \widetilde{N}_\pi(\boldsymbol{\ell})^2 \left[C_1C_1^* \left\langle \Phi_A|\Phi_A \right\rangle + C_2C_2^* \left\langle \Phi_B|\Phi_B \right\rangle + C_1C_2^* \left\langle \Phi_A|\Phi_B \right\rangle + C_1^*C_2 \left\langle \Phi_B|\Phi_A \right\rangle \right].\end{aligned} \tag{B.20}$$

Here $[C_1, C_2]$ is the eigenvector of the secular equation (B.5) for π. Both the first and second term, i.e. $C_1C_1^* \left\langle \Phi_A|\Phi_A \right\rangle$ and $C_2C_2^* \left\langle \Phi_B|\Phi_B \right\rangle$, are equal to $1/2$, since Φ_A and Φ_B are unit normalised. The two last terms of equation (B.20) can be rewritten as

$$\frac{1}{2}(e^{-i\varphi_{\boldsymbol{\ell}}} + e^{i\varphi_{\boldsymbol{\ell}}}) \left\langle \Phi_A|\Phi_B \right\rangle = s\sum_i^3 \cos\left(\varphi_{\boldsymbol{\ell}} + \mathbf{r}\cdot\mathbf{R}_i\right), \tag{B.21}$$

where $s = 0.129$ is the overlap parameter given by Hochberg et al. [20]. This results in a complete Bloch wave normalisation, with a normalisation constant given as

$$\widetilde{N}_\pi(\boldsymbol{\ell}) = \frac{(2\pi)^{3/2}}{\sqrt{1 + s\sum_i^3(\cos(\varphi_\ell + \mathbf{r}\cdot\mathbf{R}_i))}}. \tag{B.22}$$

Similar calculations can be made for the σ bands, although since the calculations are analogous with those of the π band, these are left to be performed by an interested reader. In Euclidean space, this calculation yields

$$N_\sigma(\boldsymbol{\ell}) = \frac{(2\pi)^{3/2}}{\sqrt{n_\sigma(\boldsymbol{\ell})}}, \tag{B.23}$$

where

$$\begin{aligned} n_\sigma(\boldsymbol{\ell}) =& C_1^*C_1 + C_2^*C_2 + C_3^*C_3 + 3(C_4^*C_4 + C_5^*C_5 + C_6^*C_6) \\ & 2\,\mathrm{Re}\Big[S_{\mathrm{ss}}C_1^*C_4 + S_{\mathrm{sp}}C_1^*C_5 + S_{\mathrm{sp}}C_1^*C_6 + S_{\mathrm{sp}}C_2^*C_3 + S_\sigma C_2^*C_5 + \\ & S_\pi C_2^*C_6 + S_{\mathrm{sp}}C_3^*C_4 + S_\pi C_3^*C_5 + S_\sigma C_3^*C_6 \sum_{j=1}^{3} e^{i\boldsymbol{\ell}\cdot\mathbf{R}_j}\Big]. \end{aligned} \tag{B.24}$$

The overlap parameters are presented in Table B.1.

B.2 First Brillouin Zone

The integration over the reciprocal space, $d^2\ell$, was restricted to the first Brillouin zone of a graphene crystal. Graphene has a 2D honeycomb structure with a carbon-carbon bond of length $a = 1.42\,\text{Å}$, as shown in Figure B.3. The unit vectors of the primitive cell can be defined as

$$\begin{aligned} \mathbf{a_1} &= a\frac{\sqrt{3}}{2}\left(\sqrt{3}, 1\right) \\ \mathbf{a_2} &= a\frac{\sqrt{3}}{2}\left(\sqrt{3}, -1\right). \end{aligned} \tag{B.25}$$

From this the reciprocal lattice vectors can be derived according to

$$\begin{aligned} \mathbf{b_1} &= \frac{2\pi}{a\sqrt{3}}\left(\frac{1}{\sqrt{3}}, -1\right) \\ \mathbf{b_2} &= \frac{2\pi}{a\sqrt{3}}\left(\frac{1}{\sqrt{3}}, -1\right). \end{aligned} \tag{B.26}$$

Both of these vectors have the same length given as

$$|\mathbf{b_1}| = |\mathbf{b_2}| = b = \frac{4\pi}{3a}. \tag{B.27}$$

By using this in combination with Figure B.3, the reciprocal length

$$c = \frac{4\pi}{3\sqrt{3}a} \tag{B.28}$$

can be found. From this, the first Brillouin zone is defined in the shape of a hexagon with vertices in the positions $(0, c)$, $(\frac{\sqrt{3}c}{2}, \frac{c}{2})$, $(\frac{\sqrt{3}c}{2}, -\frac{c}{2})$, $(0, -c)$, $(-\frac{\sqrt{3}c}{2}, -\frac{c}{2})$ and $(-\frac{\sqrt{3}c}{2}, \frac{c}{2})$ in Cartesian coordinates. The first Brillouin zone is shown in Figure B.3, where $\mathbf{b_1}$, $\mathbf{b_2}$ and c are presented as well.

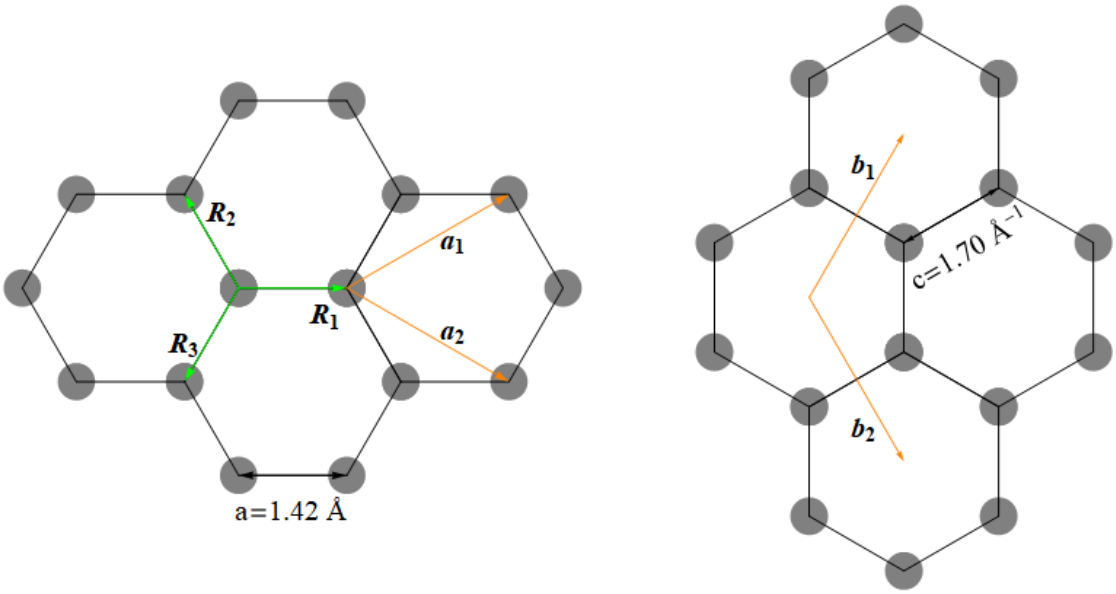

Figure B.3: Honeycomb structure of graphene (left) and the corresponding first Brillouin zone (right). On the left, $\mathbf{a_1}$ and $\mathbf{a_2}$ are the unit vectors of the primitive cell. $\mathbf{R_1}$, $\mathbf{R_2}$ and $\mathbf{R_3}$ are the vectors describing the positions of the nearest neighbours for each atom. On the right, $\mathbf{b_1}$ and $\mathbf{b_2}$ are the unit vectors of the first Brillouin zone.